High-Order Medium Frequency Micromechanical Electronic Filters

Kun Wang, *Student Member, IEEE,* and Clark T.-C. Nguyen, *Member, IEEE*

Abstract—Third-order, high-Q, micromechanical bandpass filters comprised of three ratioed folded-beam resonators coupled by flexural mode springs are demonstrated using an integrated circuit compatible, doped polycrystalline silicon surface-micromachining technology. A complete design procedure for multiresonator micromechanical filters is presented and solidified via an example design. The use of quarter-wavelength coupling beams attached to resonators at velocity-controllable locations is shown to suppress passband distortion due to finite-mass and process mismatch nonidealities, which become increasingly important on this microscale. In addition, low-velocity coupling methods are shown to greatly alleviate the lithographic resolution required to achieve a given percent bandwidth. Ratioed folded-beam micromechanical resonators are introduced as the key impedance transforming components that enable the needed low-velocity coupling. Using these design techniques, balanced three-resonator microscale mechanical filters with passband frequencies centered around 340 kHz are demonstrated with percent bandwidths of 0.1%, associated insertion losses as small as 0.1 dB, 20-dB shape factors as low as 1.5, and stopband rejections greater than 64 dB. Measurement and theory are rigorously compared and important limitations, such as thermal susceptibility, the need for passband tuning, and inadequate electromechanical coupling, are addressed. [470]

Index Terms—Circuit modeling, fabrication, electromechanical coupling, filters, high-Q, insertion loss, MEMS, microelectromechanical devices, micromachining, micromechanical, passband tuning, percent bandwidth, quarter-wavelength, resonators.

I. INTRODUCTION

VIBRATING mechanical tank components, such as crystal and SAW resonators, are widely used to implement bandpass filters in the radio frequency (RF) and intermediate frequency (IF) stages of heterodyning transceivers. Due to orders of magnitude higher quality factor Q, filters utilizing such technologies greatly outperform comparable filters implemented using conventional transistor technologies in insertion loss, percent bandwidth, and dynamic range [1]–[5]. However, being off-chip components, these mechanical devices must interface with integrated electronics at the board level, and this constitutes an important bottleneck against miniaturization and (in some cases) performance of super-heterodyne transceivers [6].

The rapid growth of micromachining technologies that yield high-Q on-chip mechanical resonators [7], [8] now suggests a method for miniaturizing and integrating highly selective filters together with transistor circuits, perhaps sowing seeds that may someday contribute towards implementation of single-chip super-heterodyne transceivers. With Q's of over 80 000 [9] under vacuum and center frequency temperature coefficients in the range of -10 ppm/°C (several times less with nulling techniques) [10], polycrystalline silicon micromechanical resonators (abbreviated "μresonators") can potentially serve well as miniaturized substitutes for crystals in a variety of high-Q oscillator and filtering applications [5], [6]. To date, two-resonator (i.e., second-order) prototypes of such filters have been demonstrated from low frequency (LF) (e.g., 20 kHz [11]) to high frequency (HF) (e.g., 8.5 MHz [12]). For use in communications, however, sharper rolloffs and larger stopband rejections are often required, and thus, much higher order must be achieved. For the majority of mechanical bandpass filter designs, the order is synonymous with the number of resonators used. However, due to increased susceptibility to passband distorting mismatches and parasitics, microscale mechanical filters utilizing three or more resonators have not yet been achieved. The present work extends the order of μmechanical filters to third [13], [14], reporting on the design, fabrication, and performance of planar integrated circuit (IC)-processed (integrated circuit), three-resonator micromechanical bandpass filters with center frequencies from 340–360 kHz, bandwidths from 400–1000 Hz (0.12%–0.28%), insertion losses as small as 0.1 dB, stopband rejections exceeding 64 dB, and 20-dB down shape factors as small as 1.5.

This paper presents the first comprehensive treatment on the design of high-order micromechanical filters. It begins with a discussion of filter insertion loss in Section II, followed by an introduction to an alternative folded-beam resonator design in Section III that utilizes ratioed supporting beam lengths to realize specified values of folding truss velocity—an essential resonator design technique that makes possible small percent bandwidth filters without the need for submicron lithographic resolution. The discussion then turns to the subject micromechanical filters, starting with qualitative descriptions of filter design and operation in Sections IV and V, followed by complete design procedures and details in Sections VI and VII, and culminating with defensive design precautions for practical implementation in Sections VIII and IX. After a brief discussion of fabrication in Section X, experimental verifications of example designs and rigorous comparison between theory and measurement then follow in Sections XI
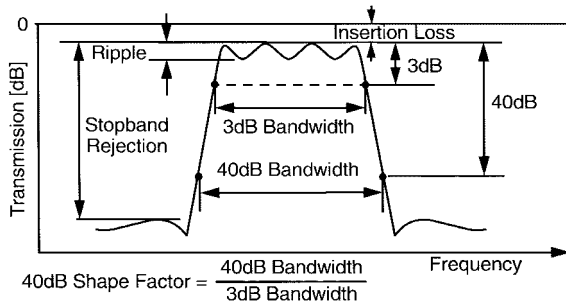
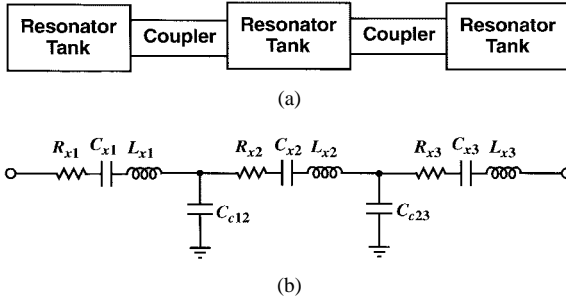Fig. 1. Parameters typically used for filter specification [15], [16].

Fig. 2. (a) A general topology for coupled resonator bandpass filters. (b) One electrical circuit implementation for the network topology of (a) using series *LCR* tanks and shunt capacitor couplers.

and XII. The paper concludes with a brief exposition on the limitations of this prototype design, followed by suggestions for overcoming them in future renditions.

II. CONTRIBUTORS TO FILTER INSERTION LOSS

Fig. 1 presents a common bandpass filter specification, explicitly indicating important metrics, such as bandwidth, insertion loss, stopband attenuation, and shape factor. Such filter characteristics are most often achieved using the network topology shown in Fig. 2(a), where several resonator tanks, each implementing a bandpass biquad function, are joined together by coupling networks [15], [16]. A specific electrical circuit implementation of this network topology using series *LCR* tanks and shunt capacitor couplers is shown in Fig. 2(b).

In the most common convention (used by discrete resonator filter designers), the order of a filter using the topology of Fig. 2(a) is equal to the number of resonators used. This is the convention taken in this paper. (Note, however, that this differs from the convention used by IC designers, who often define the filter order as being equal to two times the number of resonators.) As illustrated in Fig. 3, which plots the simulated frequency characteristics for a 455-kHz 0.2% bandwidth filter as a function of increasing filter order (i.e., increasing numbers of resonators used), the higher the order of a given filter, the sharper the rolloff and the smaller the shape factor. Thus, higher order yields better selectivity.

However, higher order also contributes insertion loss, as seen in Fig. 3. In order to suppress insertion loss in a filter with a given order and a fixed percent bandwidth, the Q of the constituent resonators should be several times higher than the quality factor of the overall filter, $Q_{\text{fltr}} = f_o/B$ (f_o is center frequency, B is bandwidth). This is illustrated in Fig. 4,
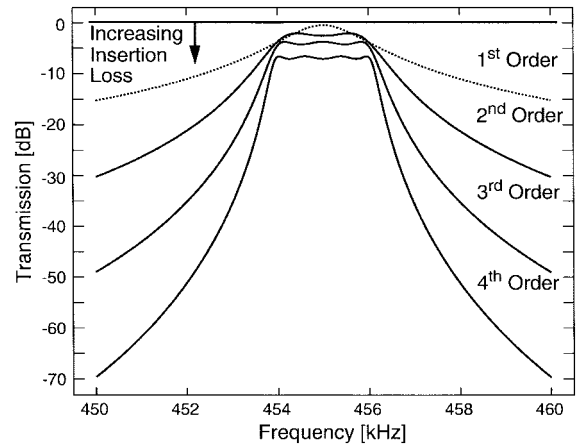

Fig. 3. Simulated frequency characteristics for a 0.2% bandwidth, 455-kHz bandpass filter as a function of increasing filter order. The resonators making up the filter had $Q = 4,400$ for these simulations.
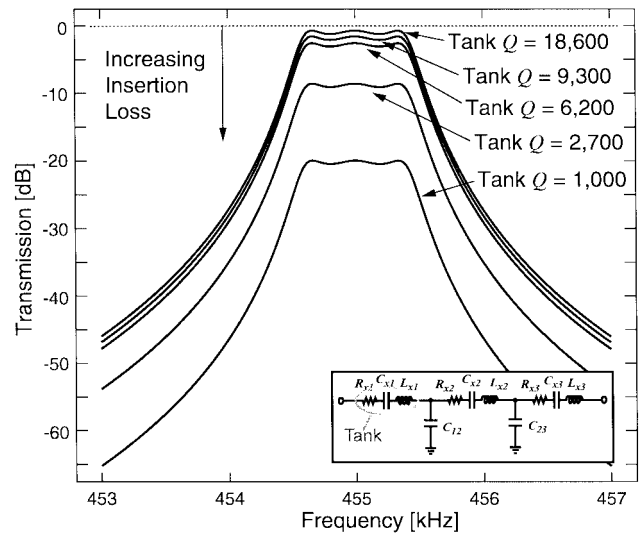

Fig. 4. Simulated frequency characteristics for a 0.2% bandwidth, three-resonator 455-kHz bandpass filter under varying tank Q's.

which plots simulated spectra for a 455-kHz filter with 0.2% bandwidth for varying values of resonator Q. For a resonator Q of 18 600, very little insertion loss is observed. However, as Q drops, insertion loss increases to the point where it exceeds 20 dB for resonator Q's less than 1000—very poor for IF filters and certainly unacceptable for RF filters.

Thus, the first requirement for achieving low insertion loss, high-order, small percent bandwidth filters is a set of constituent resonators that achieve bandpass biquad frequency characteristics with sufficiently high Q's.

III. RATIOED FOLDED-BEAM MICROMECHANICAL RESONATORS

The needed high-Q bandpass biquad spectra are regularly achieved by stand-alone micromechanical resonators, as illustrated in Fig. 5, which shows the scanning electron micrograph (SEM) of the folded-beam micromechanical resonator used in this work, along with its measured bandpass biquad frequency characteristic. The extracted Q from this plot is 41 000, which
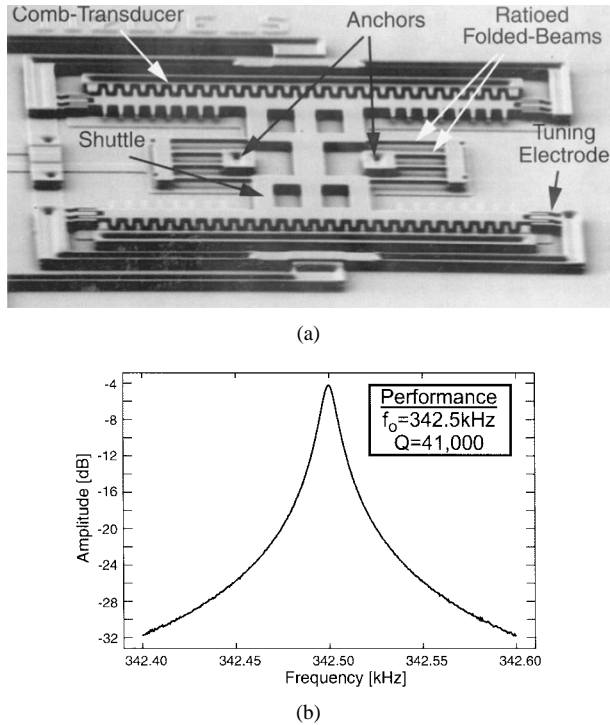
(a)

(b)

Fig. 5. (a) SEM of a ratioed folded-beam, comb-transduced micromechanical resonator (without inner electrodes). (b) Frequency characteristic for the device of (a) measured under 50 μtorr vacuum using a drive voltage of $v_i = 1$ mV and transresistance detection electronics with a gain of 100 kΩ.

is consistent with its doped polysilicon construction [17] and plenty adequate for implementation of high performance, small percent bandwidth filters. It should be stressed that this Q is achievable only in a vacuum, under pressures less than about 50 mtorr; under atmospheric pressure, gas damping becomes the dominant loss mechanism for these tiny resonators, and the Q drops by orders of magnitude [7]–[9], [18].

A. Resonator Operation

Fig. 6 presents the overhead view schematic for the micromechanical resonator of Fig. 5 in the bias and excitation configuration to be used for the end resonators in the eventual micromechanical filters. This resonator differs from previous versions [7] in two ways: 1) its inner and outer folded suspension beams are not equal in length, and 2) each electrical port (ports 1 and 2 in Fig. 6) consists of one outer and two inner resonator-to-electrode comb-capacitors, all pointing in the same direction and electrically connected to maximize the achievable electromechanical coupling. As shown, to properly excite this device [7], a voltage consisting of a dc-bias V_{Pn} ($=V_P - V_n$) and an ac excitation v_n (where n is the port number) is applied across one or more of the electrical ports. At each port, this creates a dominant force component f_{dn} between the electrode and resonator (shuttle) proportional to the product $V_{Pn}v_n$ and at the frequency of v_n given by

$$f_{dn} = -V_{Pn}\frac{\partial C_n}{\partial x}v_n \qquad (1)$$

where $(\partial C_n/\partial x)$ is the change in capacitance per unit displacement at port n. When the frequency of v_n nears the
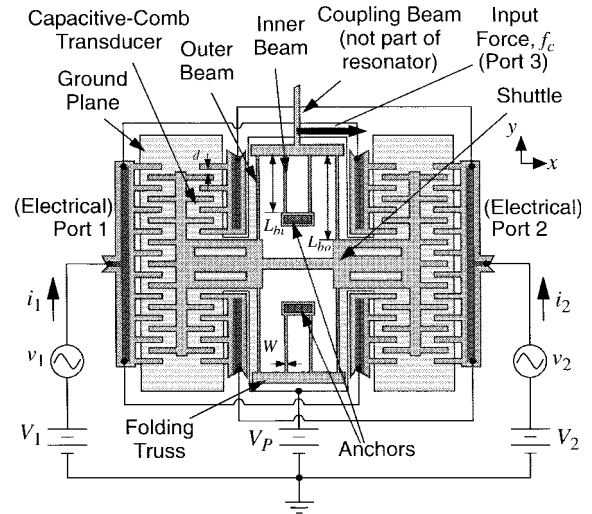

Fig. 6. Overhead-view schematic of a ratioed folded-beam, capacitive-comb transduced μmechanical resonator under a typical bias and excitation configuration. Darkly shaded regions are anchored to the substrate; lighter shading represents suspended areas. The ground plane is electrically connected to the conductive structure via the anchors.

resonance frequency, the μresonator begins to vibrate, creating a dc-biased time-varying capacitor $C_n(x, t)$ at each port. Motional currents given by

$$i_{xn} = -V_{Pn}\frac{\partial C_n}{\partial x}\frac{\partial x}{\partial t} \qquad (2)$$

are then generated through each port and serve as balanced outputs for this device. (Note that for a positive-going v_1, i_{x1} will be positive since $(\partial C_1/\partial x)$ is negative, and i_{x2} will be negative since $(\partial C_2/\partial x)$ is positive, yielding differential outputs that are balanced if the ports are symmetrical. Also, note that i_{x1} denotes a motional quantity, whereas i_1 in Fig. 6 denotes the total current into port 1 that includes both motional and static capacitor feedthrough components.) When plotted against the frequency of the excitation signal v_n, each output current i_{xn} traces out the bandpass biquad characteristic expected for a high-Q tank circuit, as shown in Fig. 5.

Note also from the discussion associated with (1) and (2) that the effective input force and corresponding output currents, respectively, can be nulled by setting $V_{Pn} = 0$ V. Thus, given input bias voltages of $V_1 = V_2 = 0$ V, a micromechanical resonator (or filter constructed of such resonators) can be switched in and out by the mere application and removal of the dc-bias voltage V_P. Such switchability can be used to great advantage in receiver architectures, which may now take advantage of large parallel arrays of switchable, highly selective micromechanical filters [6].

B. Lumped-Parameter Mechanical Equivalent Circuit

To facilitate the design and simulation of this simple single-resonator filter, and of subsequent more complicated filters using interlinked networks of resonators, equivalent lumped mechanical and electrical circuits are essential. Fig. 7 presents the mechanical equivalent circuit modeling the resonator of Fig. 6. The dynamic mass m_{rc}, stiffness k_{rc}, and damping c_{rc} at a given location c on the resonator can be derived using
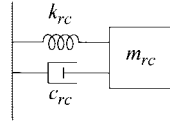
Fig. 7. Lumped-parameter mechanical equivalent circuit for the microme-chanical resonator of Fig. 6.

energy methods and are given in general by the expressions [19]

$$m_{rc} = \frac{\text{KE}_{\max}}{(1/2)v_c^2} \qquad (3)$$

$$k_{rc} = \omega_o^2 m_{rc} \qquad (4)$$

$$c_{rc} = \frac{\omega_o m_{rc}}{Q} \qquad (5)$$

where $\text{KE}_{\max}$ is the peak value of kinetic energy achieved by the system, v_c is the peak resonance velocity at location c on the resonator, and ω_o is the (radian) resonance frequency. The subscript "r" denotes a resonator quantity.

As is emphasized in Fig. 6, the ratioed folded-beam μmechanical resonator differs from previous versions [7] in that its suspending folded beams are not equal in length. Rather, the lengths of the inner and outer folded-beams are purposely ratioed to allow specification of the peak velocity at the folding truss during resonance. In attaining a specific peak resonance velocity at the folding truss, a specific dynamic mass and stiffness [as dictated by (3) and (4)] is obtained at locations on the folding truss—i.e., a specific mechanical equivalent circuit is obtained that will be "seen" by any mechanical connection attached to the folding truss. As will be detailed later, this ability to specify a desired equivalent circuit at a given location will prove essential in the design of practical micromechanical filters with small percent bandwidths.

With reference to Fig. 6, the peak resonance velocity of the folding truss v_{rt} can be specified according to

$$v_{rt} = \frac{\omega_o X_s}{1 + \beta^3} \qquad (6)$$

where X_s is the peak displacement at the shuttle mass, and

$$\beta = \frac{L_{bo}}{L_{bi}} \qquad (7)$$

is the ratio of the outer beam length L_{bo} to inner beam length L_{bi}. Using (3) and (4), the effective dynamic mass m_{rt} and stiffness k_{rt} seen at the resonator folding trusses can be expressed as

$$m_{rt} = m_{rs}\left(1 + \beta^3\right)^2 \qquad (8)$$

$$k_{rt} = k_{rs}\left(1 + \beta^3\right)^2 \qquad (9)$$

where m_{rs} and k_{rs} are the effective dynamic mass and stiff-ness, respectively, at the resonator shuttle (i.e., the maximum velocity point), given by (see Appendix A)

$$m_{rs} = M_s + \frac{M_t}{(1+\beta^3)^2} + \frac{13}{35(1+\beta^3)^2}M_{bi}$$
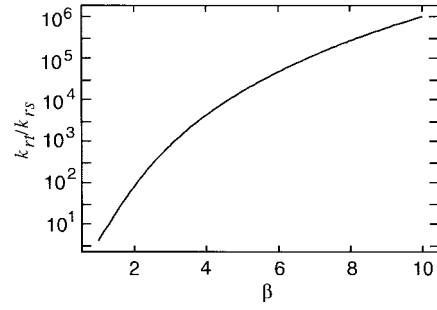$$+ \left[\frac{1}{(1+\beta^3)} + \frac{13\beta^6}{35(1+\beta^3)^2}\right]M_{bo} \qquad (10)$$

Fig. 8. Normalized effective stiffness at the folding-truss versus folded-beam ratio β.

TABLE I
MECHANICAL-TO-ELECTRICAL CORRESPONDENCE IN THE IMPEDANCE ANALOGY

Mechanical Variable	Electrical Variable
Damping, c	Resistance, R
Stiffness^{-1}, k^{-1}	Capacitance, C
Mass, m	Inductance, L
Force, f	Voltage, V
Velocity, v	Current, I

and

$$k_{rs} = \omega_o^2 m_{rs} \qquad (11)$$

where

$$\omega_o = \sqrt{\frac{k_{rs}}{m_{rs}}} = \left[\frac{4Eh(W/L_{bi})^3}{(1+\beta^3)m_{rs}}\right]^{1/2} \qquad (12)$$

is the radian resonance frequency of the resonator, derived assuming a rigid folding truss; E is the Young's modulus; h is thickness; M_s is the static mass of the shuttle; M_t, M_{bi}, and M_{bo} are the *total* folding truss, inner beam, and outer beam masses, respectively; and dimensions are defined in Fig. 6.

As seen from (6) and (7), the peak resonance velocity de-creases along the supporting beams as the location in question traverses from the shuttle mass to the anchors. It follows from (3) and (4) that relatively large dynamic masses and stiffnesses (often needed for practical filters; cf. Section VIII) can be achieved at locations near the anchors—orders of magnitude larger than achievable at the shuttle. Thus, to increase m_{rt} and k_{rt}, the folding truss must be positioned closer to the anchor—i.e., L_{bi} should be decreased, while L_{bo} is increased to maintain a constant resonance frequency, resulting in an overall increase in β. Conversely, m_{rt} and k_{rt} decrease with decreasing β. Fig. 8 plots the dynamic stiffness at the folding truss (normalized against effective stiffness at the shuttle mass) versus β, showing a full six orders of magnitude variation in stiffness for β's from 1 to 10.

C. Lumped-Parameter Electrical Equivalent Circuit

The electrical equivalent circuit for this device can be obtained using electromechanical analogies (Table I) by first identifying the number and type of ports coupling externally applied inputs and outputs to and from the μmechanical

resonator, then insuring that the electrical circuit "seen" at each port correctly models its effective impedance and its couplings with other ports.

When used in the mechanical filters to be discussed, both *electrical* and *mechanical* inputs to the μmechanical resonators are possible. Fig. 6 indicates the relevant port configuration for the end resonators in the filter design of this work. As shown, two electrical signals (i.e., voltages) are applied to the shuttle mass via capacitive comb-finger transducers, and one mechanical signal (i.e., a force f_c) located at the folding truss is supplied.

With all other ports ac-grounded, the effective impedance seen looking into a given electrical port of this μmechanical resonator may be modeled by the parallel combination of a static capacitor representing the electrode-to-resonator (and electrode-to-ground plane) capacitance present when the resonator is motionless; and a motional admittance, modeling the circuit behavior when the resonator vibrates. The static capacitor is largely overlap capacitance and may be obtained via approximate analysis, or more exactly through finite element simulation. The motional admittance at a given electrical port n in Fig. 6 is defined, in phasor form, as

$$Y_{xn}(j\omega) = \frac{I_{xn}(j\omega)}{V_n(j\omega)}. \qquad (13)$$

Using the phasor form of (2) and (13) may be expanded as

$$Y_{xn}(j\omega) = -j\omega V_{Pn}\frac{\partial C_n}{\partial x}\frac{X_s(j\omega)}{F_{dn}(j\omega)}\frac{F_{dn}(j\omega)}{V_n(j\omega)} \qquad (14)$$

where $F_{dn}(j\omega)$ is the phasor drive force imposed by v_n, and X_s is the phasor displacement of the shuttle. From (1), the phasor input voltage-to-drive force transfer function at port n is

$$\frac{F_{dn}(j\omega)}{V_n(j\omega)} = -V_{Pn}\frac{\partial C_n}{\partial x}. \qquad (15)$$

The drive force-to-displacement transfer function is given by [20]

$$\frac{X_s(j\omega)}{F_{dn}(j\omega)} = \frac{k_{rs}^{-1}}{1 - (\omega/\omega_o)^2 + j(\omega/Q\omega_o)} \qquad (16)$$

where ω_o is the natural (radian) resonance frequency, k_{rs} is the stiffness at the shuttle location, and Q is the quality factor of the resonator system. Using (15) and (16) in (14), we have for motional admittance at port n (with all other ports grounded, including any mechanical ports)

$$Y_{xn}(j\omega) = \frac{j\omega k_{rs}^{-1}V_{Pn}^2\left(\frac{\partial C_n}{\partial x}\right)^2}{1 - (\omega/\omega_o)^2 + j(\omega/Q\omega_o)}. \qquad (17)$$

Equation (17) has the form of a bandpass biquad, and thus, may be modeled by a series *LCR* circuit with element values given by

$$C_{xn} = \frac{\eta_{en}^2}{k_{rs}} \qquad R_{xn} = \frac{c_{rs}}{\eta_{en}^2} = \frac{\sqrt{k_{rs}m_{rs}}}{Q\eta_{en}^2}$$

$$L_{xn} = \frac{m_{rs}}{\eta_{en}^2} \qquad \eta_{en} = V_{Pn}\frac{\partial C_n}{\partial x} \qquad (18)$$
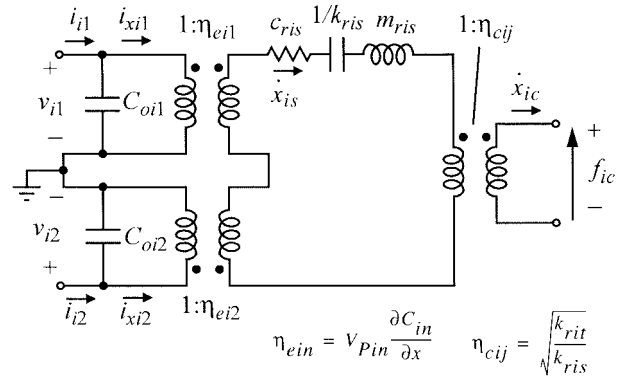

Fig. 9. Transformer-based equivalent circuit for the micromechanical resonator of Fig. 6. In the circuit, C_{oi1} and C_{oi2} denote overlap capacitance (in the rest condition), i denotes the resonator (in anticipation of the multiple resonator filters to be discussed), and n denotes the port.

at port n, where k_{rs}, m_{rs}, and c_{rs} denote values at the shuttle location. Thus, looking into an electrical port, with all other ports grounded, a series *LCR* circuit is seen (in parallel with the static capacitor C_{on}), with element values directly or inversely proportional to the mechanical circuit element values at the shuttle location modified or transformed by the electromechanical coupling parameter η_{en}. The equivalent circuit modeling the resonator and its electrical inputs can then be formulated using actual values of mass, stiffness, and damping (at the shuttle location) as the values for the inductance, capacitance, and resistance in an *LCR* circuit, and modeling electromechanical transformations from the resonator to its electrical ports by transformers [21] with η_{en}:1 turns ratios, as shown on the left-hand side of Fig. 9.

Once the shuttle is set in motion, displacements x_s on the shuttle then experience a *mechanical* impedance transformation (i.e., a velocity transformation) to the folding truss, dependent on the location of the truss relative to that of the input ports. Again, a transformer can be used to model this transformation, with turns ratio $1:\eta_c$, where from (8) and (9)

$$\eta_c = \sqrt{\frac{k_{rt}}{k_{rs}}} = 1 + \beta^3. \qquad (19)$$

In (19), the subscript "c" denotes "coupling" in anticipation of coupled-resonator filter discussions later. Fig. 9 presents the complete equivalent circuit for the end resonator of Fig. 6, incorporating both electromechanical and velocity transformers and introducing the additional subscripts i and j to specify the resonator (in anticipation of the multiple resonator filters to be discussed).

The transformer-based equivalent circuit of Fig. 9 represents a physically consistent model for the resonator of Fig. 6. It includes actual physical values for mechanical parameters, models electromechanical and mechanical transformations directly, and presents an accurate representation of mechanical (i.e., Brownian motion) thermal noise through its resistors [17], [22], [23]. In addition, it correctly models the fact that each port can influence the total resonator displacement, since the total current through the *LCR* (which represents resonator displacement) consists of (transformed) portions from each of the ports.
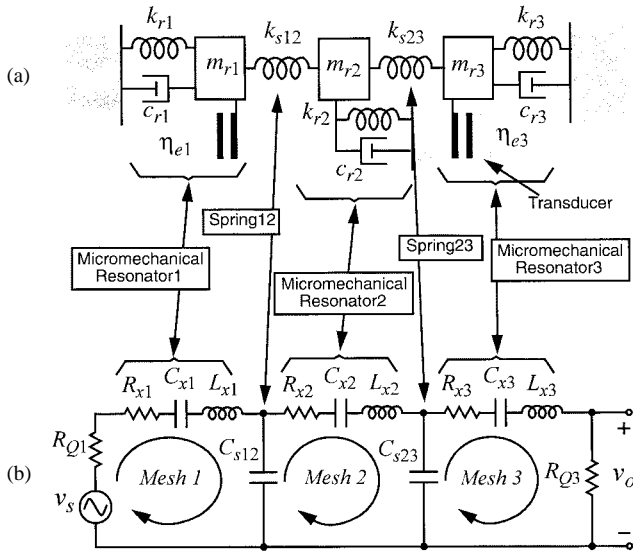
Fig. 10. (a) Equivalent lumped parameter mechanical circuit for a simple mechanical filter, with massless coupling springs. (b) Corresponding equivalent *LCR* network, with added electrical load resistors R_{Qn} and source v_s, and neglecting static capacitance at the I/O ports.

Fig. 11. Mode shapes of a three-resonator micromechanical filter and their corresponding frequency peaks.

Depending upon the type of application, parasitic capacitors coupling the electrical ports must also be added to the circuit of Fig. 9 to model feedthrough effects. These are especially important for high-frequency filters using resonators with insufficient electromechanical coupling. As will be seen in Section IX, even medium frequency (MF) filters using comb-transduction are susceptible to such feedthrough phenomena.

Typical numerical values for the elements of these equivalent circuits are given later in Section XII in association with μmechanical filter equivalent circuits.

IV. GENERAL MICROMECHANICAL FILTER DESIGN CONCEPTS

The measured spectrum of Fig. 5 represents the frequency characteristic for a two-pole bandpass filter centered at 342.5 kHz. Although useful for some applications, such as pilot tone filtering in mobile phones, two-pole filter characteristics are generally inadequate for the majority of communications applications. Rather, bandpass filters such as depicted generically in Fig. 1 are required, with flatter passbands, sharper rolloffs, and greater stopband rejections.

As discussed in Section II, the characteristic of Fig. 1 can be achieved by using more resonators. For the case of the subject μmechanical filters, a number of μmechanical resonators are coupled together by soft coupling springs [19], as illustrated schematically in Fig. 10(a) using ideal mass-spring-damper elements. By linking resonators together using networks of springs, a coupled resonator system is achieved that now exhibits several modes of vibration. As illustrated in Fig. 11 for the coupled three-resonator system of Fig. 10, the frequency of each vibration mode corresponds to a distinct peak in the force-to-displacement frequency characteristic and to a distinct, physical mode shape of the coupled mechanical resonator system. In the lowest frequency mode, all resonators vibrate in phase; in the middle frequency mode, the center resonator ideally remains motionless, while the end resonators
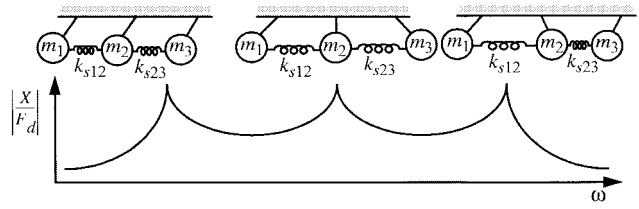
vibrate 180° out of phase; and finally, in the highest frequency mode, each resonator is phase-shifted 180° from its adjacent neighbor. Without additional electronics, the complete mechanical filter exhibits the jagged passband seen in Fig. 11. As will be shown, termination resistors designed to lower the Q's of the input and output resonators by specific amounts are required to flatten the passband and achieve a more recognizable filter characteristic, such as in Fig. 1

In practical implementations, because planar IC processes typically exhibit substantially better *matching* tolerances than *absolute*, the constituent resonators in μmechanical filters are preferably designed to be identical, with identical spring dimensions and resonance frequencies. For such designs, the center frequency of the overall filter is equal to the resonance frequency f_o of the resonators, while the filter passband (i.e., the bandwidth) is determined by the spacings between the mode peaks.

The relative placement of the vibration peaks in the frequency characteristic—and thus, the passband of the eventual filter—is determined primarily by the stiffnesses of the coupling springs (k_{sij}) and of the constituent resonators at their coupling locations (k_{rc}). In particular, for a filter with center frequency f_o and bandwidth B, these stiffnesses must satisfy the expression [15], [19]

$$B = \left(\frac{f_o}{k_{ij}} \right) \left(\frac{k_{sij}}{k_{rc}} \right) \qquad (20)$$

where k_{ij} is a normalized coupling coefficient derived from a ratio of resonance and 3-dB cutoff frequencies in a low-pass prototype for the desired filter, and easily found in filter cookbooks [15]. Equation (20) essentially derives from a denormalization of k_{ij} [15], [19]. Note from (20) that filter bandwidth is not dependent on the absolute values of resonator and coupling beam stiffness; rather, their ratio k_{sij}/k_{rc} dictates bandwidth. Thus, the general procedure for designing a mechanical filter involves two main steps (not necessarily in this order): 1) design of mechanical resonators with resonance frequencies at or near f_o and with reasonable stiffnesses k_{rc}, and (2) design of coupling springs with appropriate values of stiffness k_{sij} to achieve a desired bandwidth.

To take advantage of the maturity of *LC* ladder filter synthesis techniques, the enormous database governing *LC* ladder filter implementations [15] and the wide availability of electrical circuit simulators, realization of the μmechanical filter of Fig. 10(a) often also involves the design of an *LC* ladder version to fit the desired specification. Using the electromechanical analogies discussed in Section III and adding a source and load resistor elements, the equivalent circuit for
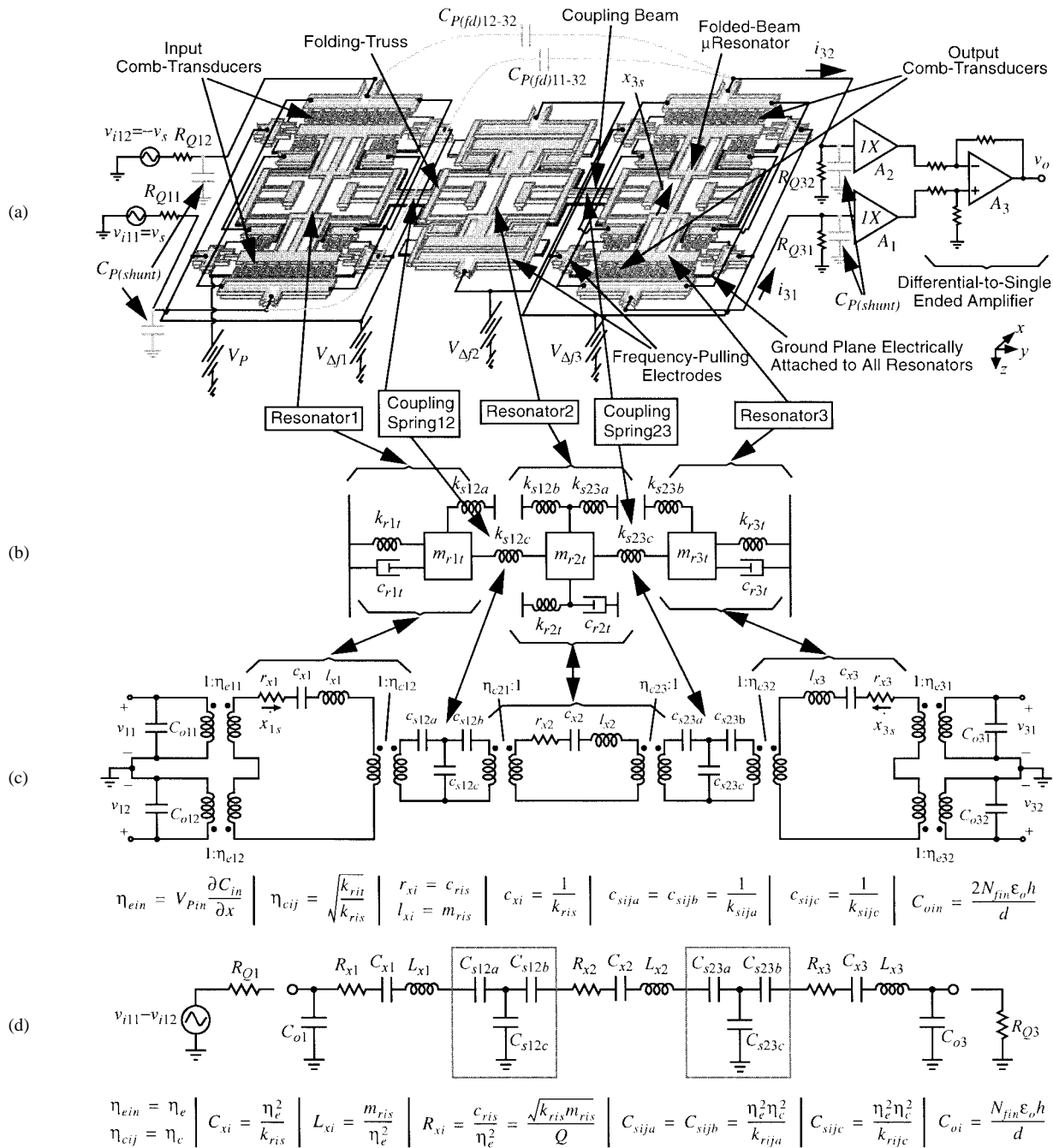
Fig. 12. (a) Schematic of a folded-beam, three-resonator, micromechanical filter with bias, excitation, and measurement circuitry. Note that only two of many $C_{P(fd)}$ capacitors are shown here to avoid clutter. (b) Mechanical equivalent circuit for the filter of (a) sans transducers. (c) Transformer-based equivalent circuit for the filter of (a). (d) One-port, impedance-explicit equivalent circuit for the filter of (a).

the mechanical system of Fig. 10(a) is shown in Fig. 10(b), which matches the generic bandpass filter circuit of Fig. 2(b) used in the general discussion of Section II.

V. PRACTICAL FILTER STRUCTURE AND OPERATION

Fig. 12(a) presents the perspective-view schematic for the three-resonator micromechanical filter [13], [14] of this work, to be described in great detail in subsequent sections. As shown in Fig. 12(b), this practical filter approximately mimics the structure of Fig. 10(a) and is comprised of three folded-

beam μmechanical resonators mechanically coupled *at their folding-trusses* by soft, flexural-mode beams (springs). The constituent resonators feature the basic ratioed folded-beam design described in Section III with the additional provision of parallel-plate capacitive transducers that allow voltage-controlled tuning of individual resonator center frequencies [24]. Since it is not involved with input/output coupling, the center resonator does not include capacitive-comb transducers; rather, it features extensive parallel-plate capacitive electrodes for enhanced frequency tuning. (In hindsight, this was not a good design strategy, since it compromised the

ability of the planar fabrication process to match resonators.) The entire μmechanical filter structure, including resonators and coupling springs, is constructed of doped (conductive) polycrystalline silicon and is suspended 2 μm over a uniform, doped-polysilicon ground plane that underlies the suspended structure at all points, electrically shielding it from the substrate. This ground plane is required to prevent electrostatic pull-in of the structure into the substrate, which can occur for structure-to-substrate voltage differences greater than 68 V.

To operate this filter, a dc-bias V_P is applied to the suspended, movable structure, while differential ac signals, v_s and $-v_s$, are applied through Q-controlling input resistors R_{Q11} and R_{Q12} to opposing ports of the input resonator, as shown in Fig. 12(a). The differential inputs applied to symmetrically opposing ports generate push–pull electrostatic forces on the input resonator, inducing mechanical vibration when the frequency of the input voltage comes within the passband of the mechanical filter. This vibrational energy is imparted to the center and output resonators via the coupling springs, causing them to vibrate as well. Vibration of the output resonator creates dc-biased, time-varying capacitors between the resonator and respective port electrodes, which source motional output currents given by

$$i_{x3n} = V_{P3n} \frac{\partial C_{3n}}{\partial x_{3s}} \frac{\partial x_{3s}}{\partial t} \qquad (21)$$

where x_{3s} is the displacement of the output resonator shuttle (defined in Fig. 12), C_{3n} is the resonator-to-electrode capacitance at port n of the output resonator (i.e., resonator 3), and V_{P3n} is the dc-bias voltage applied across C_{3n}.

The circuits used for off-chip measurement of filter characteristics are also included in Fig. 12(a). As shown, the differential output motional currents i_{x31} and i_{x32} are directed through output Q-controlling resistors R_{Q31} and R_{Q32} forming voltages across these resistors which are sensed by buffers A_1 and A_2, then directed to the differential-to-single-ended converter A_3. Note that the (A_1, R_{Q31}) and (A_2, R_{Q32}) stages could also be implemented in a transresistance fashion if each is replaced by a unity gain inverting amplifier using feedback and summing resistors equal to R_{Q3n}.

VI. MICROMECHANICAL FILTER DESIGN PROCEDURE

The design of micromechanical filters can be achieved via a procedure based to some extent on the design of generic coupled-resonator filters using tables of normalized "k and q values" found in various filter cookbooks [15], [16]. The overall design strategy is best formulated via a combination of mechanical- and electrical-domain techniques and can be enumerated in a step-by-step procedure (to be covered in detail in the next section) as follows.

1) Choose manufacturable values of coupling beam widths W_{sij}, dictated predominantly by lithographic and etch resolution.
2) Choose flexural mode coupling beam lengths L_{sij} to correspond to effective quarter-wavelengths of the filter center frequency, and evaluate the resulting stiffnesses of the coupling beams k_{sij}.

3) Choose an overall resonator shuttle geometry, leaving the number of comb-fingers per side (i.e., per electrical port) N_{fin} an open variable for later satisfaction of termination resistor R_{Qi} and dc-bias V_{Pin} requirements.
4) From the required resonator stiffnesses dictated by (20), from the mass of the chosen resonator shuttle, and using initial values of dc-bias $V_{Pin(\text{init})}$, determine simultaneously:
   a) the needed value of outer-to-inner folded beam length ratio β that achieves the necessary coupling velocity;
   b) the needed number of fingers per shuttle side to achieve the desired R_{Qi};
   c) all resonator shuttle and suspension geometries.
5) Determine the needed values of dc-biases $V_{Pin(\text{final})}$ to exactly obtain the desired values of filter termination resistance R_{Qi}.
6) Generate an electrical equivalent circuit for the filter and verify the design via simulation.

Note that in this procedure, the resonator shuttle is first chosen to satisfy the R_{Qi} requirement with assumed values of dc-bias $V_{Pin} = V_{Pin(\text{init})}$, and the exact value of $V_{Pin} = V_{Pin(\text{final})}$ needed is not determined until the end of the process, after all geometries are known.

VII. MICROMECHANICAL FILTER DESIGN DETAILS

The details for each step of the above design procedure will now be described in the context of an example. For this purpose, the 455 kHz, 400-Hz bandwidth, three-resonator micromechanical filter demonstrated in this work will be used. The design begins with specification of the coupling beam dimensions.

A. Coupling Beam Design

As indicated in the ideal circuit of Fig. 10(a), the function of the coupling beams is to implement appropriate values of stiffness to couple the resonators and achieve the needed bandwidth. The needed values of coupling spring constant k_{sij} are dictated by (20) and are obtained in large part by selecting appropriate coupling beam length and width dimensions (L_{sij} and W_{sij}, respectively) assuming a given thickness h defined by the process technology.

Although useful for illustration purposes, the mechanical filter design of Fig. 10 does not comprise a practical topology for planar-processed microscale filters, because it precludes the use of identical resonators. This is perhaps best understood in the context of the electrical equivalent to Fig. 10(a), shown in Fig. 10(b). In coupled resonator bandpass filter synthesis, elements are chosen such that each mesh (with adjacent meshes open-circuited) resonates at the center frequency f_o of the desired filter [15]. For *Mesh1*, assuming all resonators share identical masses m_{rit}'s and identical turns ratios η's (i.e., to yield identical L_{xi}'s in the electrical domain), the total capacitance resonating L_{x1} is comprised of a series combination of C_{x1} and C_{s12}. However, the total capacitance in *Mesh2* is composed of a series combination of C_{x2}, C_{s12},
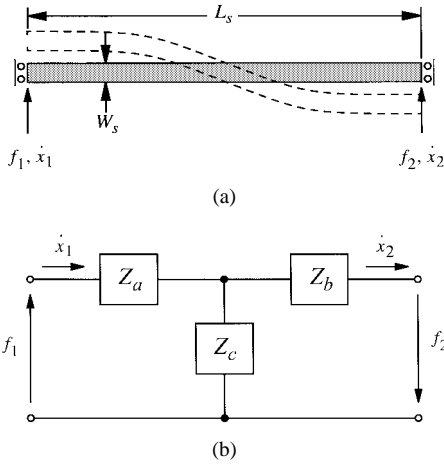
Fig. 13. (a) Coupling beam under forces f_1 and f_2 with corresponding velocity responses. (b) General transmission line T-model for the coupling beam.

and C_{s23}. Thus, *Mesh1* and *Mesh2* can resonate at f_o only if C_{x1} differs from C_{x2}; i.e., only if resonators 1 and 2 are *not* identical.

This need for nonidentical resonators constitutes an unacceptable compromise, since the resulting filter design would depend heavily on the *absolute* tolerances of the fabrication technology to achieve an undistorted passband. A design allowing identical resonators is preferable for the planar-fabricated micromechanical filters of this work, since matched resonators are much easier to achieve in a planar process than are resonators with different specific frequencies.

Designs using identical resonators are made possible by the fact that real coupling beams have finite mass, as well as stiffness, and thus actually function as acoustic transmission lines. As such, the reactance they present to adjoining resonators generally includes both mass and stiffness (i.e., inductive and capacitive) components, with values dependent upon both the dimensions of the couplers themselves and the frequency of operation. In particular, for frequencies within the filter passband, the lengths of the coupling beams correspond to specific wavelength-fractions that largely determine the impedances presented by couplers to their adjoining resonators. For example, as will be seen, coupling beam lengths less than one-eighth wavelength contribute both mass and stiffness reactances, while lengths corresponding to a quarter-wavelength at the filter center frequency present ideally zero reactances, essentially eliminating the coupling beams from mesh resonance considerations, making filter designs with identical resonators possible.

For general wavelength fractions, the coupling beam can be modeled via the T-network shown in Fig. 13(b), comprised of series mechanical impedances, Z_a and Z_b, and shunt impedance Z_c. The coupling beam dimensions yielding specific impedance values can be obtained through consideration of the impedance matrix for this flexural mode beam under fixed-fixed, sliding support boundary conditions. Via appropriate dynamical analysis, this impedance matrix takes

the form [19], [26]

$$
\begin{bmatrix} f_1 \\ \dot{x}_1 \end{bmatrix} = \begin{bmatrix} \dfrac{H_6}{H_7} & -\dfrac{2EI_s\alpha^3 H_1}{j\omega L_s^3 H_7} \\ -\dfrac{j\omega L_s^3 H_3}{EI_s\alpha^3 H_7} & \dfrac{H_6}{H_7} \end{bmatrix} \begin{bmatrix} f_2 \\ \dot{x}_2 \end{bmatrix} = \begin{bmatrix} A & B \\ C & D \end{bmatrix} \begin{bmatrix} f_2 \\ \dot{x}_2 \end{bmatrix}
$$

$$(22)$$

where

$$H_1 = \sinh\alpha\sin\alpha \qquad (23)$$

$$H_3 = \cosh\alpha\cos\alpha - 1 \qquad (24)$$

$$H_6 = \sinh\alpha\cos\alpha + \cosh\alpha\sin\alpha \qquad (25)$$

$$H_7 = \sin\alpha + \sinh\alpha \qquad (26)$$

$\alpha = L_s(\rho W_s h\omega^2/(EI_s))^{0.25}$, $I_s = hW_s^3/12$, needed dimensions are given in Fig. 13(a), and where we have assumed that rotation of the coupling beam at the connection points is not significant. This is largely the case for the design of Fig. 12(a) if finite elasticity in the folding trusses is neglected. For cases where rotation is important, the matrix in (22) becomes larger [26], but the solution methods remain similar.

Equating the circuit of Fig. 13(b) to a chain network described by (22) [15], then solving for the series and shunt impedances in terms of chain matrix elements, yields

$$Z_a = Z_b = \frac{A-1}{C} = \frac{jEI_s\alpha^3(H_6 - H_7)}{\omega L_s^3 H_3} \qquad (27)$$

and

$$Z_c = \frac{1}{C} = \frac{jEI_s\alpha^3 H_7}{\omega L_s^3 H_3}. \qquad (28)$$

The two cases of practical design interest occur when the coupling beam lengths correspond to less than one-eighth wavelength (sub-$\lambda/8$) and to an effective quarter-wavelength ($\lambda/4$) at the filter center frequency. Sub-$\lambda/8$ designs are of interest because they lend themselves more easily to lumped models and are thus analytically simpler to implement than beams with greater lengths. $\lambda/4$ designs are of great interest because they are the most robust against fabrication process variations. Each case is now individually addressed.

B. Case: $L_s < \lambda/8$

When the coupling beam length is much shorter than one-eighth of the flexural-mode wavelength corresponding to the filter center frequency, (27) and (28) reduce to

$$Z_a = Z_b = j\omega\left(\frac{M_{\text{static}}}{2}\right) = j\omega m_{sa} = j\omega m_{sb} \qquad (29)$$

where $M_{\text{static}} = \rho hW_sL_s$, and

$$Z_c = \frac{k_{sc}}{j\omega} \qquad (30)$$

where $k_{sc} = 12EI_s/(L_s^3)$. Thus, for this case, the coupling beam can be modeled as a combination of half-static-mass and stiffness elements, yielding a mechanical equivalent circuit for the filter as shown in Fig. 14(a). The addition of coupler mass to adjacent resonators is clearly seen in this equivalent circuit.
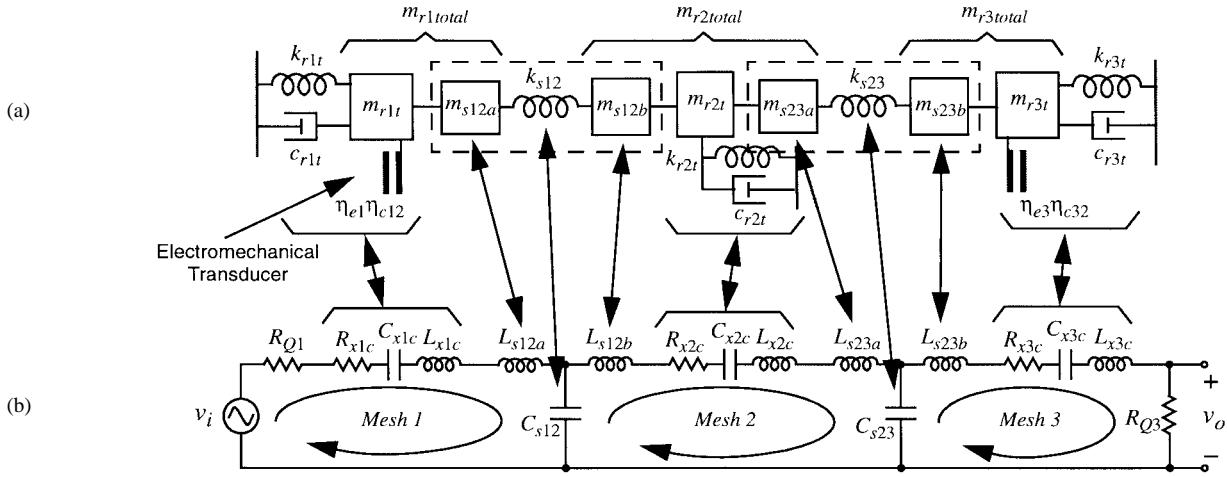
Fig. 14. (a) Lumped-parameter mechanical equivalent circuit for a micromechanical filter using coupling spring lengths much less than one-eighth wavelength of the filter center frequency. (b) Electrical equivalent circuit for the mechanical circuit of (a), including a drive source v_i and termination resistors R_{Qn}, neglecting static port capacitance, and explicitly indicating individual resonator meshes for synthesis purposes.
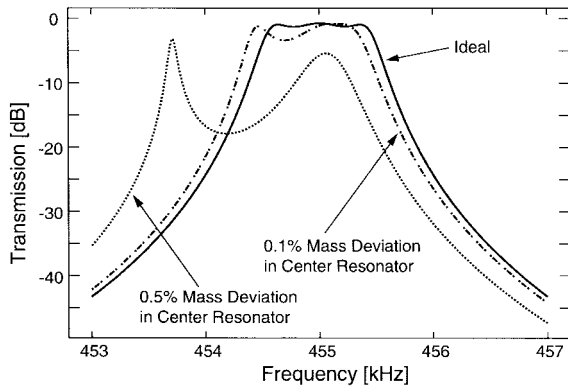

Fig. 15. Simulations demonstrating the effect of increasing center resonator mass (end resonator masses remaining constant) on the passband of a 0.2% bandwidth, 455-kHz filter.

Furthermore, note that different resonators do not receive identical mass additions. In particular, the center resonator takes on mass additions from two couplers, while the end resonators receive additions from only one each. Unless compensated out, unequal coupler mass additions to the center resonator relative to the end resonators cause mismatches in resonator frequencies, which then lead to passband distortion. Note that this phenomenon is absent for two-resonator filters, but can have a major impact on higher order filters, as illustrated by Fig. 15, which presents SPICE simulations modeling the effect of increases in center resonator mass over that of the end resonators for a three-resonator filter naively designed assuming negligible coupler mass.

The added mass from the couplers serves to partially cancel reactance contributions from their stiffnesses, allowing resonators to be more identical than allowed by the massless coupler design of Fig. 10. However, positive and negative reactance contributions from the added mass and stiffnesses do not cancel completely, so adjustments in either C_{xi} or L_{xi} (or both) for each mesh i are still required, and due to unequal L_{sij} and C_{sij} contributions for center and end resonators, these adjustments cannot be made equal for all resonators. Thus,

designs with $L_{sij} < \lambda/8$ still require nonidentical resonators to insure that all meshes resonate at f_o.

C. Case: $L_s \sim \lambda/4$

To allow the use of identical resonators, the influence of coupler reactance on mesh resonance frequencies must be eliminated. This can be achieved by choosing coupling beam dimensions such that the series and shunt arm impedances of Fig. 13(b) take on equal and opposite values, and thus, cancel in each mesh. By inspection of (27) and (28), Z_a and Z_c take on equal and opposite values when

$$H_6 = \sinh\alpha\cos\alpha + \cosh\alpha\sin\alpha = 0. \qquad (31)$$

Using the selected value of W_s (in step (1) of Section VI), (31) can be solved for the L_s that corresponds to an effective quarter-wavelength of the operating frequency. With quarter-wavelength coupler dimensions, the impedances of Fig. 13(b) are given by

$$Z_a = Z_b = \frac{EI_sH_7}{j\omega L_s^3 H_3} = \frac{k_{sa}}{j\omega} \qquad (32)$$

$$Z_c = -\frac{EI_sH_7}{j\omega L_s^3 H_3} = \frac{k_{sc}}{j\omega}. \qquad (33)$$

From these equations, with the help of (24) and (26) for expansion purposes, the stiffness of a quarter-wavelength coupling beam is found to be

$$k_{sc} = -k_{sa} = -\frac{EI_s\alpha^3(\sin\alpha + \sinh\alpha)}{L_{sij}^3(\cos\alpha\cosh\alpha - 1)}. \qquad (34)$$

Fig. 16 presents the equivalent mechanical and electrical circuits for a coupling beam with L_s corresponding to an effective quarter-wavelength of the filter center frequency. Here, only stiffness (or capacitance) is used to model both the shunt and series impedance arms to more explicitly illustrate reactance cancellation. In the equivalent mechanical circuit, equal magnitude positive- and negative-valued springs are used, which cancel one another at a given resonator coupling location when the adjacent resonator is held stationary. In the
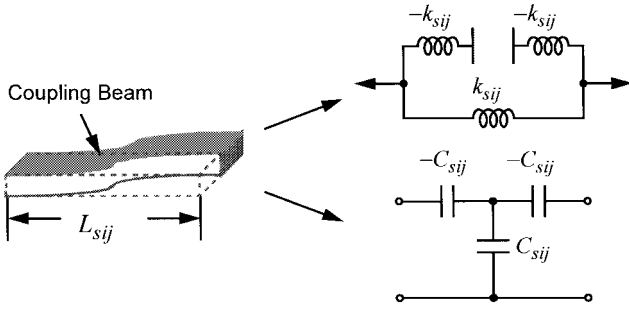
Fig. 16. Mechanical and electrical equivalent circuits for a coupling beam with dimensions corresponding to an effective quarter-wavelength of the filter center frequency. i and j denote the resonators coupled by this beam.
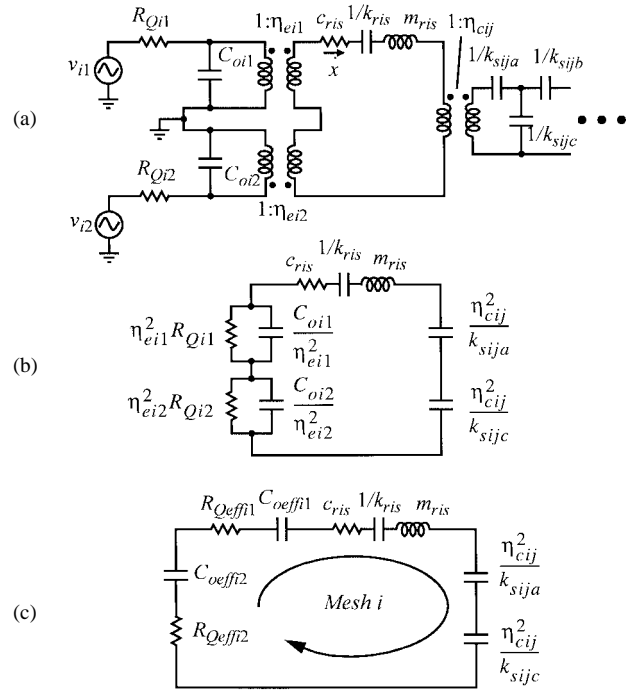

Fig. 17. (a) Relevant equivalent circuit for determining the needed value of filter termination resistance and for analyzing the effect of parasitic shunt capacitance and coupler stiffness imbalance on an end resonator. (b) Transformed version of (a). (c) Series form of (b) for mesh analysis.

corresponding electrical equivalent, the positive- and negative-valued capacitors on each side of the coupler T-network cancel one another within meshes (best seen in Fig. 12(d) with $C_{s12a} = C_{s12b} = -C_{s12c}$), and thus, do not influence the mesh resonance frequency. As a result, the resonator tanks alone dictate the resonance frequency of their respective meshes, creating a design situation where all meshes must utilize identical tank circuits to resonate at the filter center frequency f_o. This then leads to the desired result: a mechanical filter design with identical end and center resonators.

For the filter of this work, the structural thickness was set at $h = 2$ μm, and coupling beam widths W_{sij} from 1–2 μm were selected due to lithographic and etching considerations. If we further let $W_{sij} = 2$ μm for this particular example and set $k_{12} = k_{23} = 0.6474$ for a three-resonator Chebyshev filter with 0.5-dB ripple [15], (31) and (34) yield quarter-wavelength coupling beam lengths of $L_{s12} = L_{s23} = 95.5$ μm with associated stiffnesses of $k_{s12c} = k_{s23c} = 3.76$ N/m.

D. Micromechanical Resonator Specification

Having specified the coupling beam dimensions, it remains to specify geometries and dimensions for the filter resonators so that they not only resonate at the filter center frequency f_o, but also present the needed stiffness k_r to the coupling springs to satisfy (20) and attain the necessary transducer coupling to allow for a desired total termination resistance $R_{Qi} = R_{Qi1} + R_{Qi2}$ in series with ports 1 and 2 of end resonator i. Section III detailed the ratioed-folded-beam resonators to be used, which, assuming given values for structural material thickness h and suspension width W_i, are specified by the inner and outer folded-beam lengths, $L_{bi,i}$ and $L_{bo,i}$, respectively, by the number of fingers per side N_{fin} on the resonator shuttles, and by the shuttle and folding truss. Thus, to specify end resonator i, values for the parameter set $\{L_{bi,i}, L_{bo,i}, N_{fi1}, N_{fi2}\}$ must be found that simultaneously satisfy the condition set $\{R_{Qi}, f_o, k_{rit}, V_{Pi1}, V_{Pi2}\}$ needed to achieve the desired filter characteristics.

The geometry of the shuttle mass in comb-transduced micromechanical resonators is determined predominantly by the number of fingers required, which in turn is dictated by the needed value of termination resistance R_{Qi}. For a filter with center frequency f_o and bandwidth B, R_{Qi} for end resonator i is equal to the value of added series resistance needed to load its quality factor down to $q_i Q_{\text{fltr}}$ [15], where Q_{fltr} is the

quality factor of the overall filter ($Q_{\text{fltr}} = (f_o/B)$), and q_i is a normalized "q" value corresponding to the filter design in question (and easily found in filter cookbooks [15]). After transforming an end resonator circuit to explicitly show series resistance added to the resonator resistance $r_{xi} = c_{ris}$, as is done in Fig. 17, the expression for the loaded quality factor Q_{loaded} can be written

$$Q_{\text{loaded}} = Q_i \left(\frac{c_{ris}}{c_{ris} + R_{Q\,\text{eff}\,i1} + R_{Q\,\text{eff}\,i2}} \right), \qquad i = 1, 3 \quad (35)$$

where Q_i is the initial, uncontrolled quality factor of end resonator i, and

$$R_{Q\,\text{eff}\,in} = \frac{\eta_{ein}^2 R_{Qin}}{1 + (\omega_s / \omega_{QPin})^2}, \quad \text{where } \omega_{QPin} = \frac{1}{R_{Qin} C_{oin}} \quad (36)$$

and where ω_s denotes the mesh resonance frequency with parasitic capacitors included. $R_{Q\,\text{eff}\,in}$ represents the effective added series resistance from R_{Qin} after accounting for the influence of shunt capacitance C_{oin}, which can be significant if shunt parasitics are not adequately suppressed. Equating (35) to the needed $q_i Q_{\text{fltr}}$, then solving for the needed added series resistance, yields

$$R_{Q\,\text{eff}\,i1} + R_{Q\,\text{eff}\,i2} = \left(\frac{Q_i}{q_i Q_{\text{fltr}}} - 1 \right) c_{ris}, \qquad i = 1, 3. \quad (37)$$

For the purposes of simplifying this example design, and because its value is difficult to predict, interference from shunt parasitic capacitance will be neglected. (The consequences of

doing this will be revisited in Sections XI and XII.) Neglecting C_{oin}, (37) reduces to

$$\eta_{ei1}^2 R_{Qi1} + \eta_{ei2}^2 R_{Qi2} = \left(\frac{Q_i}{q_i Q_{\text{fltr}}} - 1\right) c_{ris}, \qquad i = 1, 3. \quad (38)$$

Assuming symmetrical electrical ports (i.e., $\eta_{ei1} = \eta_{ei2} = \eta_{ei}$), (38) can be further reduced to

$$\begin{aligned} R_{Qi1} + R_{Qi2} &= \left(\frac{Q_i}{q_i Q_{\text{fltr}}} - 1\right) \frac{c_{ris}}{\eta_{ei}^2} \\ &= \left(\frac{Q_i}{q_i Q_{\text{fltr}}} - 1\right) R_{xin} \\ &= R_{Qi}, \qquad i = 1, 3 \end{aligned} \quad (39)$$

where the equation for the effective series motional resistance (18) was used to obtain the final form.

To emphasize the important dependencies of the series motional resistance, the equation for R_{xin} is repeated below, and then also expressed as a function of important design variables

$$R_{xin} = \frac{\omega_o m_{ris}}{Q_i \eta_{ein}^2} = \Im_{R_{xin}}(L_{bi,i}, L_{bo,i}, N_{fi1}, N_{fi2}, V_{Pin}) \quad (40)$$

where

$$m_{ris} = \Im_{m_{ris}}(L_{bi,i}, L_{bo,i}, N_{fi1}, N_{fi2}) \quad (41)$$

$$\begin{aligned} \eta_{ein} &= V_{Pin} \frac{\partial C_{in}}{\partial x} \\ &= \Im_{\eta_{in}}(V_{Pin}, N_{fin}) \end{aligned} \quad (42)$$

$$\begin{aligned} \frac{\partial C_{in}}{\partial x} &= \frac{2\xi N_{fin} \varepsilon_o h}{d} \\ &= \Im_{\partial C_{in}/\partial x}(N_{fin}) \end{aligned} \quad (43)$$

where d is the gap spacing between electrode and resonator fingers, and ξ is a constant that models additional capacitance due to fringing electric fields [31]. From (39) and (40), we also conclude that

$$R_{Qi} = \Im_{R_{Qi}}(L_{bi,i}, L_{bo,i}, N_{fi1}, N_{fi2}, V_{Pi1}, V_{Pi2}). \quad (44)$$

The value of R_{Qi} greatly influences the magnitude of input-referred voltage noise of the filter, as well as the degree of parasitic-induced passband distortion [caused by $C_{P(\text{shunt})}$ and $C_{P(fd)}$ in Fig. 12(a)]. To minimize these effects, R_{Qi} must be minimized. From (39), this is best accomplished by minimizing the value of R_{xin} which, with reference to (40)–(43), is in turn best accomplished by maximizing $\partial C_{in}/\partial x$, assuming that V_{Pin} is restricted by power supply limitations. From (43), $\partial C_{in}/\partial x$ is best maximized by minimizing the gap spacing d between resonator and electrode comb fingers. (Note that as d decreases, N_{fin} usually increases to maintain the same overall shuttle shape, further increasing $\partial C_{in}/\partial x$.) Alternatively, if more transducer ports are available, active Q-control is also possible, which eliminates series resistors and in some scenarios can offer both noise and dynamic range advantages [9].

Another constraint that further specifies the needed geometries $\{L_{bi,i}, L_{bo,i}, N_{fi1}, N_{fi2}\}$ is the stiffness k_{rit} presented to the coupling beam by resonator i. Since coupling in this filter is done at the folding trusses, this stiffness is specified by (9), which can be rewritten to emphasize dependencies as

$$k_{rit} = \omega_o^2 m_{ris}\left(1 + \beta_i^3\right)^2 = \Im_{k_{rit}}(L_{bi,i}, L_{bo,i}, N_{fi1}, N_{fi2}). \quad (45)$$

The final constraint comes in insuring resonance at the filter center frequency, where from (12) we can also write

$$f_{oi} = f_o = \frac{1}{2\pi}\sqrt{\frac{k_{ris}}{m_{ris}}} = \Im_{f_{oi}}(L_{bi,i}, L_{bo,i}, N_{fi1}, N_{fi2}) \quad (46)$$

for resonator i.

With given values of dc-bias V_{Pi1} and V_{Pi2}, with specified values for f_o, R_{Qi}, and k_{rit}, and with an assumption of shuttle symmetry (i.e., $N_{fi1} = N_{fi2} = N_{fi}$), (44)–(46) comprise three equations in three unknowns to be solved for the needed values of $L_{bi,i}$, $L_{bo,i}$, and N_{fi}. For the present example filter design, with $f_o = 455$ kHz, $R_{Qin} = (1/2)R_{Qi} = 500$ kΩ, $k_{r1t} = k_{r2t} = k_{r3t} = k_{rit} = 6601$ N/m [determined via (20)], and $V_{Pi1} = V_{Pi2} = V_P = 150$ V, (44)–(46) yield $L_{bi,i} = 18.9$ μm, $L_{bo,i} = 29.1$ μm, and $N_{fi} = 42$ (with other parameter values summarized in Table III to be discussed in Section XI). Note that although recommended for balanced operation, shuttle symmetry need not be assumed in the solution of (44)–(46), but some relation dictating the relative values of N_{fi1} and N_{fi2} is required.

Note that the value of N_{fi} is restricted to be an integer. Thus, with the V_P used in solving (44)–(46), the value of R_{Qi} will be close to, but not exactly the desired value. To attain the specified value of R_{Qi} exactly, a slight adjustment in V_P is needed at the end of the design cycle. The final value of V_P can be obtained using the expression

$$V_{P(\text{final})} = \frac{N_{fi(\text{exact})}}{N_{fi(\text{final})}} V_{P(\text{init})} \quad (47)$$

where $N_{fi(\text{exact})}$ is the exact value of N_{fi} obtained after solving (44)–(46), $N_{fi(\text{final})}$ is the rounded integer value, and $V_{P(\text{init})}$ is the value of V_P used to solve (44)–(46). From (47), $V_{P(\text{final})}$ is found to be 147.2 V for $R_{Qin} = 500$ kΩ. Although used in actual testing for this work, these values are clearly excessive. Methods for reducing them will be discussed later.

E. Complete Filter Design Summary

The parameters derived above along with other relevant parameters for this example filter are summarized in the "Designed" subcolumn of the $\beta = 1.53$ design in Table III in Section XI. Note that the design summary for a $\beta = 1$ filter is also included in Table III, as are measured and adjusted values to be discussed in Sections XI and XII. The designs in this work and data in Tables III–V were generated automatically by a custom-coded computer-aided-design (CAD) program that closely implements the design procedures of this section. Given a typical input specification summarized by Fig. 1, this CAD package generates both geometric data and SPICE circuit simulation netlists for a micromechanical

filter conforming to the design of Fig. 12. This approach to design and verification of the subject micromechanical filters demonstrates their amenability to CAD-based implementation, perhaps on a massive scale in future applications.

F. Equivalent Circuit for the Designed Filter

By combining the equivalent circuit concepts discussed in Section III and earlier in this section, the transformer-based equivalent circuit for the overall filter is generated and presented in Fig. 12(c), along with equations for the element values. Numerical values for the circuit elements corresponding to the above filter designs (for $\beta = 1$ and $\beta = 1.53$) are determined using data from Table III, then summarized in the "Designed" columns of Table IV in Section XII. "Adjusted" values are also given, to be explained and used in Section XII for simulation verification of actual measurements.

Note that although each of these filters is designed to achieve quarter-wavelength couplers, the equivalent circuit in Fig. 12(c) does not outright assume equivalent magnitude shunt and series arms in the coupling beam T-networks. This is to maintain enough flexibility to also allow for modeling of filters that have been altered by process variations during fabrication. The circuits, however, still retain the use of capacitive T-networks, rather than inductor/capacitor networks.

For a filter designer, the transformer-based circuit of Fig. 12(c) does not lend itself well to quick, intuitive inspection analysis. For example, the resistance R_{xin} seen looking into an electrical port—crucial in setting the needed value of termination resistance in μmechanical filters, as seen in (39)—is not readily seen in the circuit of Fig. 12(c). Thus, this circuit has been simplified via transformation of all elements to the input, yielding an impedance-explicit equivalent circuit in Fig. 12(d) that lends itself more readily to inspection circuit analysis. Element values for this circuit are given in Table V.

VIII. IMPORTANCE OF LOW-VELOCITY COUPLING

The filter designed in the previous section can be termed a "(7/32)-velocity coupled" or "$(7/32)v_{max}$ coupled" filter, in that spring coupling occurs at folding truss locations that in this design [using $\beta = 1.53$ in (6)] are moving at approximately 7/32 the velocity of the shuttle mass v_{max}. (Recall that the shuttle mass moves at the highest velocity in the system.) Thus, this design clearly utilizes the low velocity coupling strategy described in Section III.

It should be stressed that the range of percent bandwidths achievable by micromechanical filters would be very small if not for the concept of low velocity coupling. In particular, without the impedance transformation afforded by low velocity coupling, the spring widths required to achieve percent bandwidths less than 0.15% are in the submicron regime. For example, if constituent resonators were constrained to have equal inner and outer folded-beams (i.e., constrained to half-velocity coupling, meaning coupling at points moving at half the velocity of the shuttle mass), then the resonator stiffness at the truss coupling location would be constrained to a constant. For the case of a $(1/2)v_{max}$ coupled 455-kHz filter,
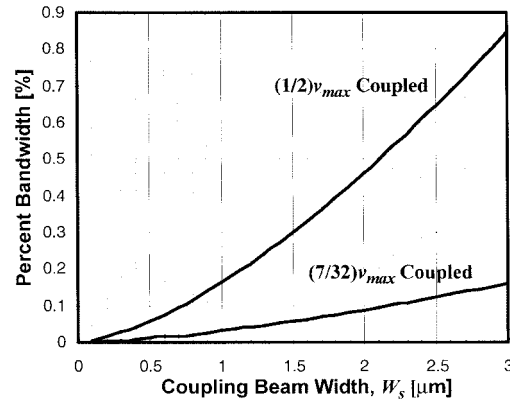

Fig. 18. Plots of percent bandwidths achievable by coupling beam widths that satisfy quarter-wavelength requirements for a 455-kHz three-resonator μmechanical filter using $(1/2)v_{max}$ and $(7/32)v_{max}$ coupling.

with k_{rit} constrained to 1258 N/m, the percent bandwidths (B/f_o) achievable via coupling beam widths (W_{sij}'s) that satisfy both quarter-wavelength and (20)'s requirements are plotted in Fig. 18. Here, submicron dimensions are shown to be necessary for percent bandwidths lower than 0.16% for the half-velocity coupled case.

The use of lower velocity coupling (e.g., $(7/32)v_{max}$) allows much larger values of k_{rit}, allowing correspondingly larger values of k_{sij}, and in turn larger values of W_{sij} for a given percent bandwidth. For comparison with the $(1/2)v_{max}$ coupled case, data for a $(7/32)v_{max}$ coupled filter ($k_{rit} = 6,601$ N/m) are also included in Fig. 18. Note how the $(7/32)v_{max}$ coupled design avoids submicron widths down to 0.04% bandwidth—much smaller than achievable by its $(1/2)v_{max}$ counterpart.

Through a combination of coupling beam width and coupling location, a wide range of achievable percent bandwidths is available for a given filter. In particular, coupling beam width can be used to set a nominal bandwidth, with coupling location setting the range of bandwidths achievable around that nominal value. For example, for a 455-kHz filter with a structural layer thickness of 2 μm and with 2-μm-width coupling beams, the stiffness variation for β ranging from 0.5 to 1.5 (a rather conservative range) corresponds to a range of percent bandwidths from 0.1% to 1.4%. With 3-μm-width coupling beams, percent bandwidths from 0.18% to 2.5% are achievable over the same range of β.

In addition to the above, an equally important advantage of low-velocity coupling is its ability to decrease the sensitivity of the overall filter to coupler mass deviations caused by process variations that pull coupling beam dimensions away from quarter-wavelength values. This comes about because, as dictated by (8), not only stiffness, but mass as well is increased via low-velocity coupling, and a plot similar to that of Fig. 8 showing orders of magnitude increases can also be made for mass. Thus, by using low-velocity coupling techniques to increase resonator masses, the percent change in resonator mass caused by unbalanced coupler mass additions (such as shown in Fig. 14) can be greatly reduced, leading to an overall filter response that is much more resilient against process variations.
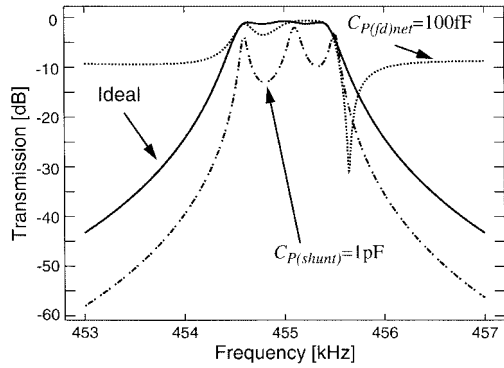
Fig. 19. SPICE simulations illustrating the effect of shunt and feedthrough parasitic capacitance on the filter passband. See Fig. 12(a) for parasitic capacitor definitions. Here, $C_{P(fd)\text{net}} \approx C_{P(fd)12-13} - C_{P(fd)11-32}$ represents the net uncancelled port-to-port feedthrough capacitance.

Fig. 20. Cross section of the polysilicon surface-micromachining technology used in this work.

TABLE II
DOPING RECIPES

POCl$_3$	Implant
(i) Deposit 2 μm LPCVD fine-grained polysilicon @ 588°C	(i) Deposit 1 μm LPCVD fine-grained polysilicon @ 588°C
(ii) Dope 2.5 hrs. @ 950°C in POCl$_3$ gas	(ii) Implant phosphorous: Dose=10^{16} cm^{-2}, Energy=90 keV
(iii) Anneal for 1 hr. @ 1100°C in N$_2$ ambient	(iii) Deposit 1 μm LPCVD fine-grained polysilicon @ 588°C
	(iv) Anneal for 1 hr. @ 1100°C in N$_2$ ambient

IX. PRACTICAL IMPLEMENTATION ISSUES

In addition to the above theoretical issues, practical design issues, such as resiliency against fabrication mismatch and against parasitic elements, must also be considered. Fig. 15 from Section VII showed that even slight mismatches between constituent resonators can lead to significant passband distortion. In addition, as shown in Fig. 19, parasitic capacitance shunting and connecting the filter inputs and outputs can also greatly distort the passband. In particular, shunt capacitance can not only alter end mesh frequencies, but can also interact with Q-controlling resistors to cause excessive phase lag, which then distorts the passband and can preclude termination-based passband-flattening.

To correct for fabrication mismatch tolerances and input/output parasitic interference, each resonator comprising the filter is equipped with parallel-plate-capacitor transducers, which due to their displacement-to-capacitance nonlinearity, allow frequency tuning of resonators via inherent voltage-dependent electrostatic spring constants [24], given by

$$k_{eis} = -(V_P - V_{\Delta fi})^2 \frac{C_{o\,\text{tune},i}}{d_{\text{tune},i}^2}. \tag{48}$$

In (48), $C_{o\,\text{tune},i}$ is the tuning electrode-to-resonator overlap capacitance given (for the end resonators) by

$$C_{o\,\text{tune},i} = \frac{2\xi_{\text{tune},i} N_{\text{tune},i} \varepsilon_o h L_{o\,\text{tune},i}}{d_{\text{tune},i}} \tag{49}$$

where $N_{\text{tune},i}$ is the total number of tuning electrodes, $\xi_{\text{tune},i}$ is a fringing field factor for the tuning finger overlap capacitance, and $d_{\text{tune},i}$ and $L_{o\,\text{tune},i}$ are the tuning electrode-to-resonator gap spacing and overlap length, respectively. Note that the presence of gaps on both sides of the shuttle tuning fingers does not alter their function; i.e., electrical stiffnesses do not cancel in symmetric configurations [25]. The dependence of frequency on tuning voltage $V_{\Delta fi}$ for resonator i then follows readily from (48) and (49), and is given by

$$f'_{oi} = \frac{1}{2\pi}\sqrt{\frac{k_{ris}}{m_{ris}}} = \frac{1}{2\pi}\sqrt{\frac{k_{mis}+k_{eis}}{m_{ris}}} = f_{o\,\text{nom}}\left(1+\frac{k_{eis}}{k_{mis}}\right)^{1/2} \tag{50}$$
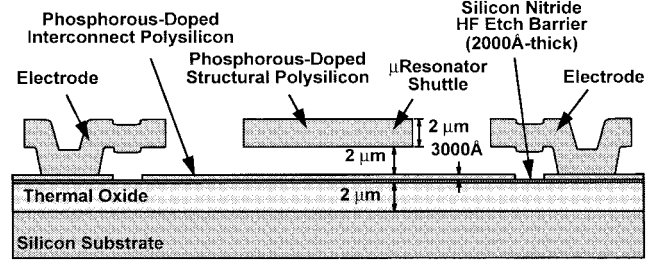
where k_{mis} is the nominal *mechanical* stiffness at the shuttle location (with $k_{eis} = 0$), and $f_{o\,\text{nom}}$ is the nominal resonance frequency (again, with $k_{eis} = 0$). The principles behind (50) will be used extensively to correct measured passbands in Section XI.

To minimize the effects of parasitic feedthrough capacitance $C_{P(fd)}$, the differential drive and sense scheme depicted in Fig. 12(a) is utilized, where currents feeding through capacitors $C_{P(fd)12-32}$ and $C_{P(fd)11-32}$ cancel to first order at output port 32. Also, for the experimental demonstration to be covered in Section XI, input and output shunt capacitance is minimized by careful board layout of off-chip electronics.

X. FABRICATION

Several prototype MF micromechanical bandpass filters with various coupling velocities and percent bandwidths (including the one from Section VII) were designed using the methods detailed in Sections VI, VII, and IX, then fabricated using a three-mask, polysilicon, surface-micromachining technology [7] with the cross section shown in Fig. 20. Stand-alone ratioed folded-beam resonators were also fabricated to investigate characteristics of individual resonator devices. As shown in Fig. 20, the substrate in this process was not doped beyond the starting wafer doping (10-Ω-cm resistivity); i.e., there is effectively no substrate ground plane in this process. In addition, two different methods for depositing and doping the polysilicon structural material were utilized to investigate the effect of the doping procedure on resonator Q: one based on POCl$_3$-doping, and the other on implant-doping. Table II summarizes the exact deposition and doping recipes used for each case. Note from the table that the structural polysilicon is
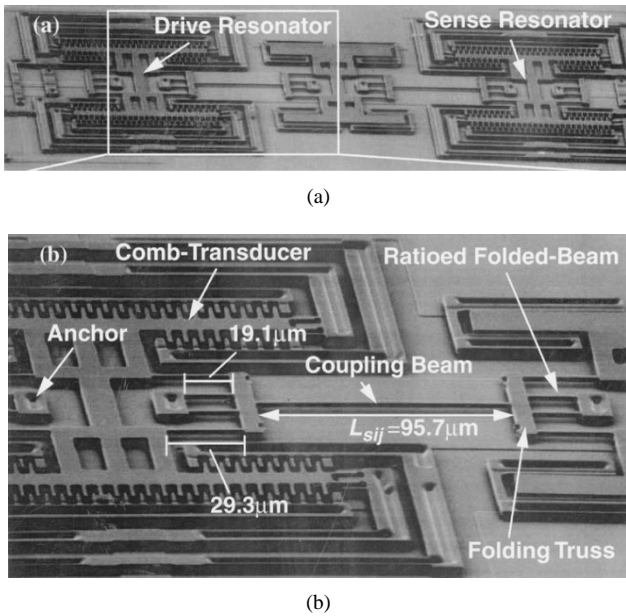
Fig. 21. SEM's of a fabricated ratioed folded-beam micromechanical filter. (a) Full view. (b) Enlarged partial view.

Fig. 22. Measured transconductance spectra (under 20-mtorr pressure) for (a) a $POCl_3$-doped resonator and (b) an implant-doped version, both after furnace annealing.

deposited at a temperature optimized to yield low-stress, fine-grained characteristics [27]. The grains are grown, however, during the subsequent dopant drive-in anneals, which are chosen to attain an acceptable compromise between structural film stress and conductivity.

Fig. 21(a) and (b) presents the full- and zoomed-view SEM's, respectively, of the $(7/32)v_{max}$ coupled three-resonator filter designed in Section VII and summarized in Tables III–IV. The use of unequal folded-beam lengths for low velocity coupling is clearly seen in the figure.

XI. EXPERIMENTAL RESULTS

A custom-built vacuum chamber, with pc board support and feedthroughs allowing electrical connections to external instrumentation, was utilized to characterize both μmechanical resonators and filters. Devices under test were bonded to carefully grounded metal platforms and interfaced with surface-mounted off-chip electronics at the board level, taking special precautions to minimize shunt capacitance at the filter input and output nodes and to null out feedthrough capacitance as much as possible. A turbomolecular pump was utilized to evacuate the chamber to pressures on the order of 50 μtorr before testing devices.

A. Stand-Alone Ratioed Folded-Beam Resonators

Stand-alone, ratioed folded-beam, comb-driven μmechanical resonators [as in Fig. 5(a)] were tested first, using the described vacuum chamber along with op-amp based transresistance amplifiers (with $R_{gain} = 100$ kΩ) and an HP 4195A Network/Spectrum Analyzer [17]. Differences in Q were immediately observed between $POCl_3$- and implant-doped resonators. As shown in Fig. 22, implant-doped resonators consistently exhibited several times higher Q's, with values often exceeding 40 000—some with Q's up to 60 000—under pres-
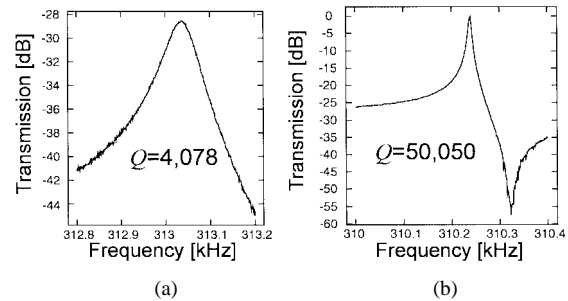
sures below 20 mtorr. The $POCl_3$-doped resonators, on the other hand, exhibited Q's of only 4000 under the same measurement conditions, and with the same annealing cycles. These results, combined with observations of increased polysilicon surface roughness after $POCl_3$-doping, suggest Q-limiting loss mechanisms dominated by surface defects [28]. Given the above observations, all results to be described in this section correspond to implant-doped devices.

The μmechanical resonator measured in Fig. 5, which posts a resonance frequency of 342.5 kHz, was actually designed to resonate at 455 kHz. The observed 24.7% frequency discrepancy arises as a result of both design and process imperfections. Specifically, the analytical resonance frequency equation (12) was derived assuming that the folding trusses were much more rigid than folded-beams attached to them. Thus, although (12) is accurate for sub-100-kHz resonators with folded-beam lengths in excess of 60 μm—much more compliant than their associated folding trusses—it is not entirely correct for the 455-kHz resonators of this work, which feature folded-beam lengths below 30 μm. In fact, two-dimensional finite-element analysis (FEA) using the commercial package IDEAS clearly shows finite elasticity in the folding trusses during resonator operation and reveals a resonance frequency 7.4% lower than predicted by (12) for the device of Fig. 5.

The absolute frequency is further decreased by process deviations that compromise resonator dimensions. In particular, both lithographic limitations and undercutting during etching led to 0.1–0.2-μm decreases in device dimensions. To further complicate matters, observed undercuts varied not only from wafer to wafer, but also along axes; i.e., lines along one axis ending up 0.1 μm thinner than designed may be 0.2 μm thinner along a perpendicular axis. It should be understood that such variations are more severe than normally encountered in a state-of-the-art semiconductor fabrication facility. With proper defensive design—e.g., accounting for undercuts in advance—in a better controlled facility, absolute frequency tolerances well below that seen in this work should be achievable.

As described in Section IV, the passband stability of a micromechanical filter is heavily dependent upon the matching tolerance of its fabrication process. The average resonance frequency mismatch in the present process for four resonators in close proximity was found to be 0.7%, which is somewhat
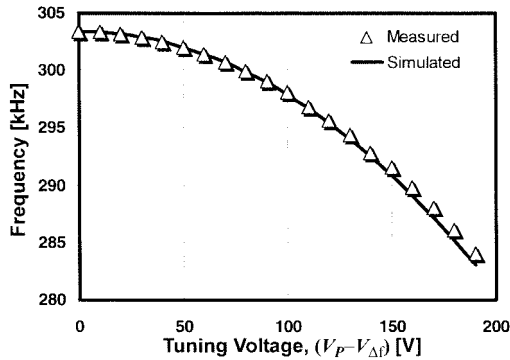
Fig. 23. Measured and simulated plots of resonance frequency versus tuning voltage for a stand-alone end-resonator with $d_{\text{tune},i} = 1 \ \mu$m and $C_{\text{tune},i} = 2.5$ fF ($\xi_{\text{tune},i} = 1.095$).

Fig. 24. Plots of fractional frequency versus temperature for a $(7/32)v_{\max}$ ratioed-beam μresonator and a $(1/2)v_{\max}$ equal-beam μresonator measured under 50-μtorr vacuum with linear resonance amplitudes.

worse than the 0.4% of a previous run [29]. This degree of frequency mismatch is sufficient to cause significant passband distortion in filters and, as will be seen, must be corrected using trimming or tuning strategies to obtain a given filter specification.

To demonstrate the frequency tuning range provided by the parallel-plate capacitor tuning structures described in Section IX, Fig. 23 presents a plot of resonance frequency versus tuning voltage $V_{\Delta f}$ for a stand-alone end-resonator, measured using the described setup, along with the theoretical prediction of (50). Here, a tuning range of over 2% is demonstrated for a 0–100-V range in $V_{\Delta f}$—quite adequate for compensation of measured mismatches—and close agreement between measurement and prediction is observed.

The thermal dependence of the constituent resonators is also of interest, since frequency changes caused by temperature shifts will also lead to filter center frequency shifts, or even passband distortion. In particular, the thermal stability of ratioed folded-beam resonators may be in question relative to their equal-beam counterparts, because the unequal inner and outer folded-beam lengths of the former expand differently with temperature. Such an expansion difference can generate suspension stress (and associated f_o shifts) if the substrate thermal expansion coefficient differs significantly from that of the structural material. Fig. 24 compares the measured fractional frequency versus temperature plots for a $\beta = 1.53$ ratioed folded-beam resonator with an equal-beam-length version. As shown, the ratioed folded-beam resonator is in fact less susceptible to temperature variations than its equal beam counterpart, with a total fractional frequency variation -564.4 ppm (compared with -1165.3 ppm for the equal beam case) over the 80 °C measurement range. The measured curves show an almost linear decrease in frequency with increasing temperature, with corresponding temperature coefficients of -7.8 ppm/°C and -15.6 ppm/°C for the ratioed- and equal-beam designs, respectively.

The improved thermal stability of the ratioed-beam resonator is attributed to the introduction of stress in its suspensions that counteract the thermal dependence of Young's modulus. This result also suggests some degree of mismatch between the coefficients of thermal expansion of the silicon substrate and the polysilicon structure.
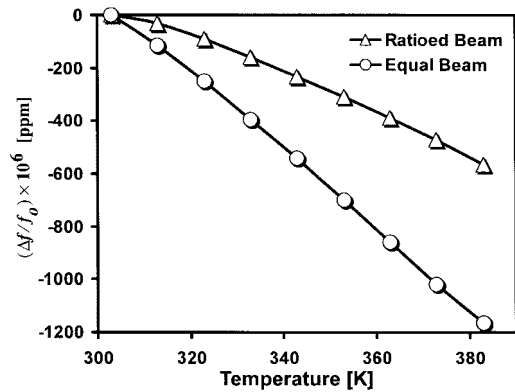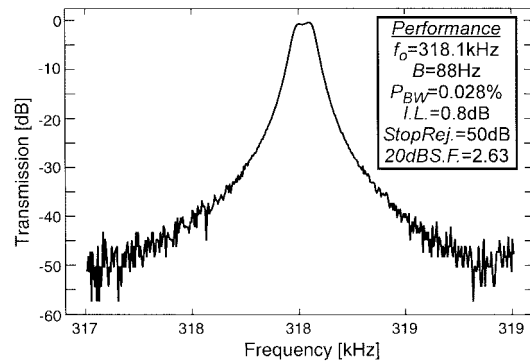

Fig. 25. Transmission spectrum for a 318.1 kHz, 88.4-Hz bandwidth, two-resonator micromechanical filter.

B. Micromechanical Filters

Micromechanical filters were then characterized, again using the custom-built vacuum chamber, with board-level electronics hooked up as in Fig. 12(a). Two-resonator filters were tested first for later comparison with higher order versions. Fig. 25 presents the transmission spectrum for a two-resonator filter, showing a center frequency of 318.1 kHz, a bandwidth of 88.4 Hz (with $R_{Qi1} = R_{Qi2} = 47$ kΩ), 20-dB and 40-dB shape factors of 2.63 and 8.22, respectively, and an insertion loss of 0.8 dB. Characterization of three-resonator filters was then accomplished using the following procedure.

1) Measure the as-fabricated frequency characteristic with only 10-kΩ termination resistors (so each mode is distinctly visible).
2) Tune resonance frequencies via $V_{\Delta fi}$'s to achieve symmetrical modal frequencies.
3) Then insert proper values of R_{Qin} to flatten the filter passband to the specified ripple.

The measured transmission spectra for the $(7/32)v_{\max}$ coupled ($\beta = 1.53$) micromechanical filter designed in Section VII, after each step of this procedure, are presented in Fig. 26. Note from this figure that due to process mismatches, the frequency characteristic of the filter looks very little like the desired response immediately after fabrication [Fig. 26(a)]. The observed degree of mismatch is more than expected from just the process variations described earlier. Rather, the passband dis-
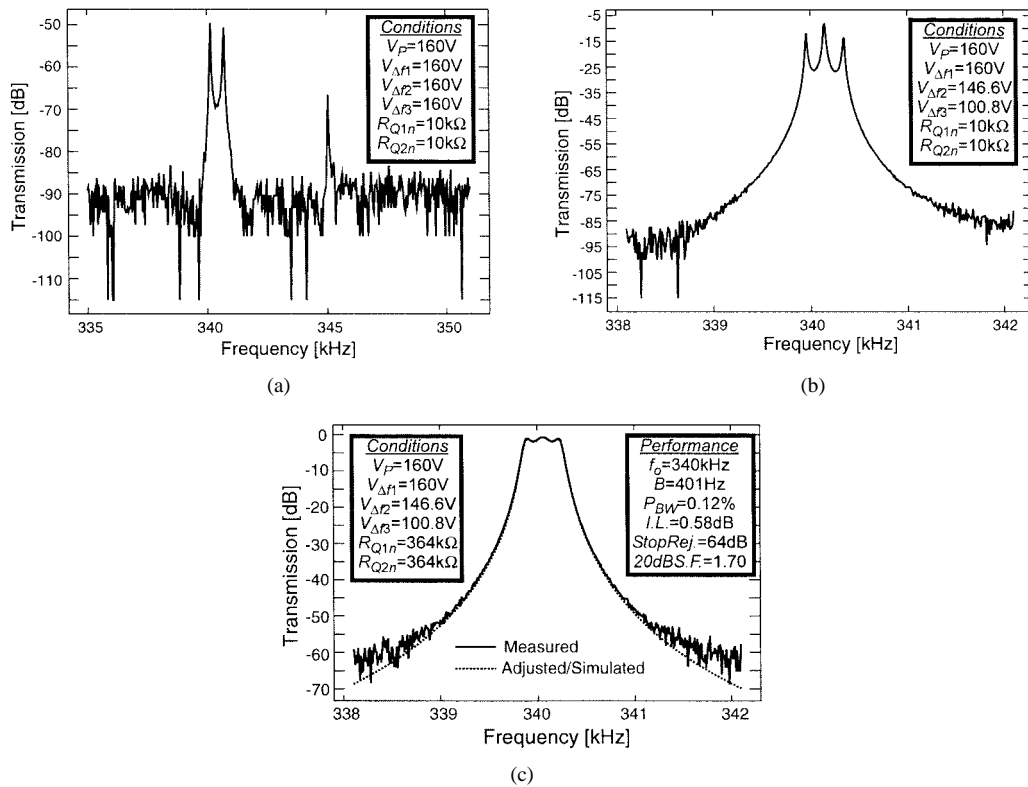
Fig. 26.   Measured transmission spectra for the prototype, three-resonator, $(7/32)v_{\max}$ coupled, micromechanical filter (a) immediately after fabrication, (b) after frequency tuning to achieve matched resonators, and (c) after passband correction using Q-controlling resistors.

tortion is exacerbated by the fact that although it was designed to resonate at the same frequency as its neighbors, the center resonator was not physically identical to the end resonators. In particular, the center resonator lacks the interdigitated comb-fingers of the end resonators, so its definition is not influenced by the same finger-derived lithographic and etch variations that affect the patterning of the end resonators. As a result, its mass differs significantly from that of the end resonators, leading to a difference in resonance frequency, and in turn, to consequential passband distortion. In retrospect, for closer uncompensated matching of resonators immediately after fabrication, the center resonator should have been designed to be identical to the end resonators, interdigitated fingers and all, regardless of whether inputs/outputs are needed.

Thus, post-fabrication tuning was essential to successful implementation of this filter. For this work, tuning was performed by varying $V_{\Delta fi}$ voltages applied to tuning fingers [cf. Fig. 12(a)], one resonator at a time, while simultaneously monitoring the frequency characteristic on a network analyzer to achieve the frequency characteristic of Fig. 26(b), in which the peaks are equidistant from one another. Automatic tuning techniques using intelligent transistor circuitry would certainly be beneficial in future filter implementations. It should be noted that although changes in $V_{\Delta fi}$ can generate absolute shifts in peak position, there is only one bandwidth (and one set of $V_{\Delta fi}$'s) at which the peaks are equidistant. As a result, $V_{\Delta fi}$ cannot be used to vary the filter bandwidth without distorting the passband. Fig. 26(c) presents the final filter spectrum after proper termination using the termination resistor values of Table III.
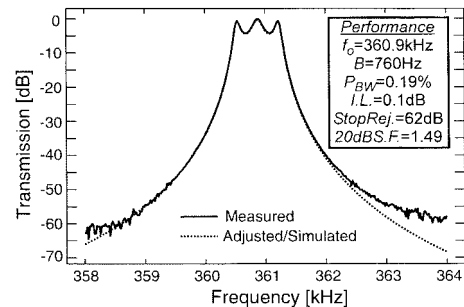
Fig. 27.   Measured frequency characteristic for a half-velocity coupled, three-resonator, micromechanical filter, along with a matched characteristic obtained via simulation.

Designed and measured data for the $(7/32)v_{\max}$ coupled filter of Fig. 26 are summarized in the "Designed" and "Measured" columns of Table III. Ignoring for a moment the large discrepancy in center frequency, the measured spectrum of Fig. 26(c) still achieves many of the intended design specifications, including a bandwidth of 401 Hz (0.12% bandwidth), insertion loss less than 0.6 dB, 20-dB and 40-dB shape factors of 1.70 and 3.48, respectively, and a stopband rejection greater than 64 dB. Ignoring for now the large dc voltages and impedances required to achieve it, this frequency characteristic rivals that of many macroscopic high-Q filters, including crystal filters, which are some of the best available [30].

For later comparative evaluation in Section XII, the measured frequency characteristic for a half-velocity coupled filter (also summarized in Table III) is presented in Fig. 27. This filter achieves similar performance, with a measured charac-

TABLE III
MF Micromechanical Filter Design Test and Simulation Verification Summary

Parameter	$v_c = (1/2)v_{max}$ (β=1)			$v_c = (7/32)v_{max}$ (β=1.53)			Units
	Designed	Measured	Adjusted/Simulated	Designed	Measured	Adjusted/Simulated	
Center Frequency, f_o	455	360,900	360,880	455	340,060	340,060	kHz
Bandwidth, B	981	760	763	400	401	403	Hz
Percent Bandwidth, (B/f_o)	0.22	0.19	0.21	0.088	0.12	0.12	%
Insertion Loss, IL	0.26	0.1	0.44	0.6	0.58	0.57	dB
20dB Shape Factor	1.77	1.49	1.49	1.75	1.70	1.66	—
40dB Shape Factor	3.68	2.97	2.86	3.61	3.48	3.33	—
Stopband Rejection, SR	∞	62.4	∞	∞	64.0	∞	dB
Passband Ripple, PR	0.5dB	4.25	4	0.5dB	1.25	1.3	dB
Normalized q_1=q_2	1.8636	—	1.8636	1.8636	—	1.8636	—
Normalized k_{12}=k_{23}	0.6474	—	0.6474	0.6474	—	0.6474	—
Frequency Modification Factor, γ	—	—	0.92554	—	—	0.9262	—
μRes. Folded-Beam Length, L_{bo}	24.8	24.9-25.0	**25.0**	29.1	29.2-29.3	**29.3**	μm
μRes. Folded-Beam Length, L_{bi}	24.8	24.9-25.0	**25.0**	18.9	19.0-19.1	**19.1**	μm
Folded-Beam Ratio, β	1	1	1	1.53	1.53	1.53	—
μRes. Folded-Beam Width, W_r	2	1.8-1.9	**1.84**	2	1.8-1.9	**1.76**	μm
Structural Layer Thickness, h	2	2	2	2	2	2	μm
Resonator Mass @ Shuttle, m_{ris}	3.85×10^{-11}	—	3.92×10^{-11}	3.76×10^{-11}	—	3.82×10^{-11}	kg
Resonator Stiffness @ Shuttle, k_{r1s}	314.8	—	201.25	307.0	—	174.27	N/m
Resonator Stiffness @ Shuttle, k_{r2s}	314.8	—	201.30	307.0	—	174.27	N/m
Resonator Mass @ Truss, m_{rit}	1.54×10^{-10}	—	1.57×10^{-10}	8.1×10^{-10}	—	8.12×10^{-10}	kg
Resonator Stiffness @ Truss, k_{r1t}	1,258	—	805.0	6,601	—	3,703.5	N/m
Resonator Stiffness @ Truss, k_{r2t}	1,258	—	805.2	6,601	—	3,703.5	N/m
No. Fingers Per Side, N_{fi}	42	42	42	42	42	42	—
Comb-Finger Gap Spacing, d	1	1	1	1	1	1	μm
Comb-Finger Overlap, L_o	5	5	5	5	5	5	μm
$\|\partial C_{in}/\partial x\|$ Per Side	1.49×10^{-9}	—	1.63×10^{-9}	1.49×10^{-9}	—	1.63×10^{-9}	F/m
$\partial C_{in}/\partial x$ Modification Factor, ξ	1	—	1.095	1	—	1.095	—
μresonator Q at 50 μTorr	40,000	~40,000	40,000	40,000	~40,000	40,000	—
Young's Modulus, E	150	150	150	150	150	150	GPa
Density of Polysilicon, ρ	2,300	2,300	2,300	2,300	2,300	2,300	kg/m^3
Coupling Beam Length, L_{s12}=L_{s23}	74.6	74.7-74.8	**74.8**	95.5	95.6-95.8	**95.7**	μm
Needed L_{s12}=L_{s23} at this f_o	74.6	—	78.1	95.5	—	107.7	μm
Coupling Beam Width, W_{s12}=W_{s23}	1.22	1-1.1	**1.06**	2	1.8-1.9	**1.9**	μm
Coupling Beam Stiffness, k_{s12a}=k_{s23a}*	-1.79	—	-0.97	-3.76	—	-1.96	N/m
Coupling Beam Stiffness, k_{s12c}=k_{s23c}†	1.79	—	1.11	3.76	—	2.86	N/m
Filter Design DC-Bias, $V_{P(init)}$	150	—	—	150	—	—	V
Filter Needed DC-Bias, $V_{P(final)}$	148.6	170	170	147.2	160	160	V
Shunt Parasitic Capacitance, C_{Pin}	0	~700	700	0	~700	700	fF
No. Tuning Fingers, N_{ftune}	8	8	8	8	8	8	—
Tuning Finger Gap Spacing, d_{tune}	1	1	1	1	1	1	μm
Tuning Finger Overlap, L_{otune}	8	8	8	8	8	8	μm
μRes1 Freq. Tuning Voltage, $(V_P-V_{\Delta f1})$	0	0	**40.2**	0	0	**13.8**	V
μRes2 Freq. Tuning Voltage, $(V_P-V_{\Delta f2})$	0	37.4	**39.9**	0	13.4	**13.7**	V
μRes3 Freq. Tuning Voltage, $(V_P-V_{\Delta f3})$	0	86.5	**40.2**	0	59.2	**13.8**	V
Q-Control Resistors, R_{Q1n}=R_{Q3n}‡	1,300	474(648)	474	500	364(369)	364	kΩ

* Obtained using (27).   † Obtained using (28).   ‡ Number in ( ) is needed value.

teristic centered at 360.9 kHz, a bandwidth of 760 Hz (0.19% bandwidth), an associated insertion loss of 0.1 dB, 20-dB and 40-dB shape factors of 1.49 and 2.97, respectively, and a stopband rejection exceeding 62 dB.

C. Filter Temperature Dependence

Fig. 28 presents frequency characteristics for a $(7/32)v_{max}$ coupled filter measured under three different temperatures: 27 °C, 77 °C, and 127 °C. Although the center frequency of this 0.12% bandwidth filter is seen to decrease at the rate of 6.1 ppm/°C, and the bandwidth at the rate of 564 ppm/°C (with a 22-Hz total bandwidth change over the 100

°C measurement range), the passband shape remains relatively intact over the full 100 °C temperature range. This relatively constant passband shape should simplify future temperature compensation approaches based on feedback control of the $V_{\Delta fi}$ voltages in Fig. 12(a).

D. Micromechanical Filter Spurious Response

Fig. 29 presents the frequency characteristic of a $(7/32)$ v_{max} coupled filter measured over a wide range of frequency, from 1 to 5 MHz. Although the stopband level rises somewhat at higher frequencies due to board-level parasitic feedthrough effects, there are no observable spurious responses.
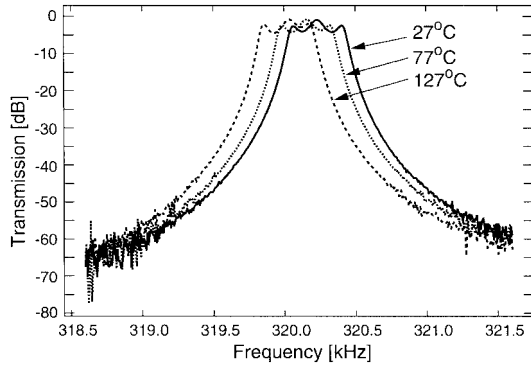
Fig. 28. Frequency characteristics for a $(7/32)v_{\max}$ coupled μmechanical filter measured under various temperatures.
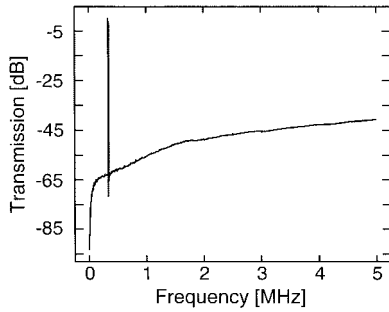

Fig. 29. Measured frequency characteristic for a $(7/32)v_{\max}$ coupled μmechanical filter measured over a wide frequency range in search of spurious responses.

XII. MEASUREMENT VERSUS THEORY

To verify the design theory of Sections III–IX, and to obtain further insight into practical filter dependencies, circuit models were generated to match the measured spectra of Figs. 26(c) and 27 via simulation. In order to match measured and simulated spectra, several adjustments were made to the original design data in the "Designed" columns of Table III to account for both process variations and model deficiencies. The adjusted parameters are summarized in the "Adjusted/Simulated" columns of Table III, with major adjustments indicated in boldface. The resulting element values for the circuit models of Fig. 12(c) and (d) used for eventual simulation verification are given in the "Adjusted/Simulated" columns of Tables IV and V, respectively. Note that after appropriate adjustments, the measured and simulated passbands and shape factors are virtually identical in Figs. 26(c) and 27, with the only discrepancies coming in the stopband, where unmodeled parasitic feedthrough capacitance $C_{P(fd)}$ raises the stopband level over the simulated prediction. Specific adjustments and their justifications are now addressed one by one.

A. Center Frequency

Discrepancies between the resonance frequency values in the "Designed" and "Measured" columns of Table III were previously attributed to both deficiencies in (12) and process variations in Section XI. To account for rigid truss modeling deficiencies, (12) is multiplied by a factor γ, which matches the frequency obtained in (12) to that found via FEA simulation.

TABLE IV
455-kHz μMECHANICAL FILTER TRANSFORMER-BASED
EQUIVALENT CIRCUIT [cf. FIG. 12(c)] ELEMENT SUMMARY

Parameter	$v_c = (1/2)v_{max}$ (β=1)		$v_c = (7/32)v_{max}$ (β=1.53)		Units
	Designed	Adjusted/ Simulated	Designed	Adjusted/ Simulated	
$C_{o11}=C_{o12}=C_{o31}=C_{o32}$	7.44	8.14	7.44	8.14	fF
$l_{x1}=l_{x2}=l_{x3}$	3.85×10^{-11}	3.92×10^{-11}	3.76×10^{-11}	3.82×10^{-11}	H
$c_{x1}=c_{x3}$	0.00318	0.00497	0.00326	0.00574	F
c_{x2}	0.00318	0.00497	0.00326	0.00574	F
$r_{x1}=r_{x3}$	2.75×10^{-9}	2.22×10^{-9}	2.68×10^{-9}	2.04×10^{-9}	Ω
r_{x2}	2.75×10^{-9}	2.22×10^{-9}	2.68×10^{-9}	2.04×10^{-9}	Ω
$c_{s12a}=c_{s23a}$	−0.559	−1.027	−0.266	−0.509	F
$c_{s12b}=c_{s23b}$	−0.559	−1.027	−0.266	−0.509	F
$c_{s12c}=c_{s23c}$	0.559	0.899	0.266	0.349	F
$\eta_{e11}=\eta_{e12}=\eta_{e31}=\eta_{e32}$	2.21×10^{-7}	2.77×10^{-7}	2.19×10^{-7}	2.61×10^{-7}	C/m
$\eta_{c12}=\eta_{c21}=\eta_{c23}=\eta_{c32}$	2	2	4.64	4.61	—

TABLE V
455-kHz μMECHANICAL FILTER IMPEDANCE-EXPLICIT
EQUIVALENT CIRCUIT [cf. Fig. 12(d)] ELEMENT SUMMARY

Parameter	$v_c = (1/2)v_{max}$ (β=1)		$v_c = (7/32)v_{max}$ (β=1.53)		Units
	Designed	Adjusted/ Simulated	Designed	Adjusted/ Simulated	
$C_{o1}=C_{o2}$	3.72	4.07	3.72	4.07	fF
$R_{x1}=R_{x3}$	56.31	28.95	55.96	30.03	kΩ
R_{x2}	56.31	28.953	55.96	30.031	kΩ
$L_{x1}=L_{x2}=L_{x3}$	787.9	510.8	783.0	562.3	H
$C_{x1}=C_{x3}$	0.155	0.381	0.156	0.390	fF
C_{x2}	0.155	0.381	0.156	0.390	fF
$C_{s12a}=C_{s23a}$	−109.1	−314.9	−274.6	−735.2	fF
$C_{s12b}=C_{s23b}$	−109.1	−314.9	−274.6	−735.2	fF
$C_{s12c}=C_{s23c}$	109.1	275.8	274.6	503.9	fF

Although not a rigorous correction, the parameter γ serves its purpose for the present discussion, which focuses more on filter passband and rolloff shape than on the absolute center frequency.

To account for process variations, undercuts within the specified measured ranges are incorporated into various dimensions in the "Adjusted/Simulated" columns of Table III and emphasized with boldface font. The values chosen here are those most frequently measured via zoomed SEM methods for the respective filter types.

B. Passband Shape

A very important consequence of the observed frequency deviations is that the coupling beam lengths no longer correspond to quarter-wavelengths of the operating frequency. Table III includes values for the fabricated coupling beam lengths (determined using the 455-kHz design frequency) and the lengths actually *needed* for quarter-wavelength coupling at the measured operating frequency. Note that the $(1/2)v_{\max}$ coupled design essentially retains quarter-wavelength couplers, but the $(7/32)v_{\max}$ coupled design deviates significantly from quarter-wavelength. As will be seen, however, the passband of the $(7/32)v_{\max}$ coupled filter actually suffers very little from this due to its use of low-velocity coupling, which makes its resonators look more massive (cf. Section VIII), effectively

reducing the influence of coupler mass additions generated by nonquarter-wavelength behavior.

As discussed in Section IX, parasitic capacitance also contributes to passband distortion. Due to a combination of symmetrical electrical ports and careful board layout, the measured feedthrough capacitance $C_{P(fd)}$ in this system was too small to influence the filter passband. The shunt capacitance $C_{P(\text{shunt})}$, on the other hand, was measured to be about 700 fF, which is large enough to cause significant passband distortion, especially for the 0.12% bandwidth $(7/32)v_{\max}$ coupled filter.

Some insight into the mechanisms by which these nonidealities distort the passband can be obtained by determining the frequency-pulling voltages required to restore the passband to its proper shape (or at least to place mode frequencies at the proper locations). To this end, Fig. 17(a) presents the relevant portion of the equivalent circuit for the case under discussion, where parasitic shunt capacitance is directly modeled, and nonquarter-wavelength couplers are modeled by unequal T-network capacitor magnitudes. For ease of analysis, this circuit is further transformed to the simpler network in Fig. 17(b), then to the series impedance network in Fig. 17(c).

As discussed in Section VII, constraints associated with filter synthesis demand that end *Meshi* (with all other meshes open-circuited) resonates at the center frequency f_o of the filter. This in turn requires that the total reactance around the *Meshi* loop vanishes at f_o. Expressing this as an equation yields (51), shown at the bottom of the page, where the equivalent capacitors

$$C_{o\,\text{eff}\,in} = \frac{1 + (\omega_o/\omega_{QP})^2}{\eta_{ein}^2 R_{Qin}(\omega_o/\omega_{QP})^2} \qquad (52)$$

have been defined to model the transformed series reactances at ω_o from the $C_{oin} - R_{Qin}$ combinations. Expressing the resonator stiffness k_{ris} as the sum of a mechanical stiffness k_{mis} and the electrical stiffness k_{eis} defined by (48), then solving (51) for k_{eis} yields

$$k_{eis} = \omega_o^2 m_{ris} - k_{mis} - \frac{1}{C_{o\,\text{eff}\,i1}} - \frac{1}{C_{o\,\text{eff}\,i2}} - \frac{k_{sija}}{\eta_{cij}^2} - \frac{k_{sijc}}{\eta_{cij}^2}. \qquad (53)$$

This equation gives the value of k_{eis} needed to negate the asymmetric passband distorting effects of shunt input capacitance C_{oin} and unbalanced k_{sija} and k_{sijc} stiffnesses caused by nonquarter-wavelength coupling.

Applying (48) to (53), the expression for the needed tuning voltage for end resonator i is obtained as in (54), shown at the bottom of the page. A similar derivation yields the corresponding expression for the center resonator

$$(V_P - V_{\Delta fi}) =$$
$$\left\{ \frac{d_{\text{tune},i}^2}{C_{o\,\text{tune},i}} \left(k_{mis} - \omega_o m_{ris} + \frac{k_{sija}}{\eta_{cij}^2} + \frac{k_{sijc}}{\eta_{cij}^2} \right) \right\}^{1/2},$$
$$i = 2 \qquad (55)$$

where there is enhanced dependence on nonquarter-wavelength effects, but no dependence on input capacitance C_{oin}.

Equations (54) and (55) were used to generate the $(V_P - V_{\Delta fi})$ values indicated in the "Adjusted/Simulated" columns of Table III and were instrumental in achieving the undistorted passbands in the simulated curves of Figs. 26(c) and 27. For the purposes of determining $(V_P - V_{\Delta fi})$ values, the center resonators were assumed identical to the end resonators. In reality, they were not [cf. Fig. 12(a)], but this way the amount of tuning required to compensate for nonquarter-wavelength and parasitic effects is readily apparent in the difference between center and end resonator $(V_P - V_{\Delta fi})$'s. In this light, the larger deviation in center resonator $(V_P - V_{\Delta fi})$ from that of the end resonators for the $(1/2)v_{\max}$ coupled filter relative to the $(7/32)v_{\max}$ coupled one indicates that under these ideal conditions (i.e., no process mismatches), the shunt parasitic capacitive hindrances of the former have a larger passband distorting effect than the nonquarter-wavelength deficiencies of the latter. This is consistent with the observation that the lower-velocity coupling of the $(7/32)v_{\max}$ coupled filter desensitizes its passband against coupler mass additions caused by nonquarter-wavelength behavior.

Note that although these correcting voltages help to maintain passband symmetry in the presence of substantial parasitic interference, they do not eliminate increases in capacitance-induced ripple, which actually arise from termination resistance deficiencies described by (36).

C. Termination Resistance

As previously mentioned, the needed value of total termination resistance R_{Qi} is strongly dependent upon the $(\partial C_{in}/\partial x)$ of the end resonator ports, given by (43). Of the variables in (43), the theoretical parameter ξ, which models the effect

$$\frac{1}{j\omega_o C_{o\,\text{eff}\,i1}} + \frac{1}{j\omega_o C_{o\,\text{eff}\,i2}} + \frac{1}{j\omega_o(1/k_{ris})} + j\omega_o m_{ris} + \frac{1}{j\omega_o\left(\dfrac{\eta_{cij}^2}{k_{sija}}\right)} + \frac{1}{j\omega_o\left(\dfrac{\eta_{cij}^2}{k_{sijc}}\right)} = 0 \qquad (51)$$

$$(V_P - V_{\Delta fi}) = \left\{ \frac{d_{\text{tune},i}^2}{C_{o\,\text{tune},i}} \left(k_{mis} - \omega_o m_{ris} + \frac{1}{C_{o\,\text{eff}\,i1}} + \frac{1}{C_{o\,\text{eff}\,i2}} + \frac{k_{sija}}{\eta_{cij}^2} + \frac{k_{sijc}}{\eta_{cij}^2} \right) \right\}^{1/2}, \qquad i = 1, 3 \qquad (54)$$

of fringing electric fields, is the most uncertain. Although extensive treatments to determine ξ can be found [31], these methods have so far not accounted for levitation effects [32], and thus, lead to unreasonable values for ξ. In particular, for the comb geometries used here (1-μm gaps, 2-μm-wide fingers, offset 2 μm above the ground plane), the theory of [31] yields $\xi = 2.44$, which is much higher than the value of 1.095 determined via measurements of $\partial C/\partial x$ on several stand-alone resonators and used in the "Adjusted/Simulated" columns for both the $(7/32)v_{\max}$ and $(1/2)v_{\max}$ coupled filters. The well-behaved passband and the close agreement between measured and simulated curves in Fig. 26(c) serves as further verification that $\xi = 1.095$ is indeed the appropriate value, at least for the $(7/32)v_{\max}$ coupled filter. Note that $\xi = 1.095$ was also used for the $(1/2)v_{\max}$ coupled filter, and this actually yielded a needed R_{Qin} value of 648 kΩ for this filter. Due to excessive phase lag caused by $C_{P(\text{shunt})}$, this value of R_{Qin} could not be used for the actual measurement; rather, a compromise of 474 kΩ was used, which resulted in more ripple than desired, but which retained some integrity in the passband. Nevertheless, even under these conditions, Fig. 27 shows good agreement between passband ripple magnitudes obtained via model simulation using $\xi = 1.095$ and measurement, providing further confidence in this value for ξ.

D. Bandwidth

Using the T-network model for coupling beam impedance, along with (27) and (28), bandwidth variations can be accounted for entirely by the aforementioned etch undercuts in coupling beams and resonator folded-beams.

It should be noted from the "Designed" and "Measured" columns of Table III that the $(1/2)v_{\max}$ coupled filter using $\sim$1-μm-wide coupling beams was able to more closely match its target percent bandwidth (within 14%) than its $(7/32)v_{\max}$ coupled counterpart using $\sim$2-μm-wide coupling beams, which missed its target by 36%. This might at first seem counterintuitive, since one might expect the filter using the wider coupling beams to be less susceptible to process variations. The poorer stability for the $(7/32)v_{\max}$ coupled filter in fact actually arises from the slower undercut rate for coupling springs ($\sim$0.1-μm average undercut) than for folded-beams ($\sim$0.2-μm average undercut) described in Section XI. With these unequal undercut rates, the coupling and folded-beam widths for the $(1/2)v_{\max}$ coupled filter scaled by about the same factor, which allowed this particular design to retain quarter-wavelength coupling and to retain the designed k_{sijc}/k_{rit} ratio, both of which impact the filter bandwidth. For the $(7/32)v_{\max}$ coupled filter, on the other hand, coupling and folded-beam widths scaled by quite different factors, significantly changing k_{sijc}/k_{rit} ratios and throwing off quarter-wavelength coupling, giving rise to the ensuing bandwidth discrepancy. Again, all of this is a result of nonuniform undercutting along wafer axes; had the undercutting been more uniform, the $(7/32)v_{\max}$ coupled filters might have shown the better bandwidth stability.

Thus, these bandwidth results should not be used to evaluate the effectiveness of low velocity coupling. Rather, the advantages of low velocity coupling should be recognized with the observation that even though the $(7/32)v_{\max}$ coupled filter uses coupling beam widths almost twice as large as its $(1/2)v_{\max}$ coupled counterpart, it still achieves a smaller percent bandwidth.

E. Practical Performance Issues

Although impressive frequency characteristics for fabricated micromechanical filters have been demonstrated, a more pragmatic inspection of Table III reveals some remaining practical implementation issues. Perhaps the most offensive of these are the large values of termination resistance R_{Qin} (100's of kΩ) and dc-bias voltage V_P ($\sim$170 V) required. Such generous values of voltage are not available in the vast majority of communication subsystems, particularly compact, mobile ones. Furthermore, an R_{Qi} as large as $2 \times (364 \text{ k}\Omega) = 728$ kΩ not only amplifies problems with parasitic capacitance, as dictated by (36), but also generates 150 nV/$\sqrt{\text{Hz}}$ of input-referred voltage noise. In addition, matching considerations become complicated with R_{Qin} values this large.

Strategies to reduce both R_{Qin} and V_P are required. Among the most promising are: 1) decreasing the electrode-to-finger gaps and 2) fully integrating the filter with sense electronics. The latter approach minimizes parasitic capacitance, allowing the use of larger R_{Qin} values (if noise permits), while drastically reducing the required value of V_P. Of the above two strategies, decreasing the gap spacing is perhaps the most direct and can be achieved via more aggressive lithography combined with high density plasma etching [33], or by making vertical resonators with electrode-to-resonator gaps defined by sacrificial spacers rather than lithography [6], [12].

In addition to the above electrical issues, numerous practical implementation issues remain, such as methods for low-cost vacuum encapsulation and low-voltage techniques for frequency trimming and tuning. Fortunately, this micromechanical filter is just one of many MEMS applications that require either vacuum encapsulation or hermetic sealing for protection against the environment. Fueled by this common need among many applications, various approaches to low-cost, chip-level, vacuum encapsulation have recently been demonstrated, some using planar processing to achieve sealable caps [34], and others using wafer-scale bonding methods [35]. Improvements to each of these approaches are ongoing. On the other hand, methods for large-scale frequency trimming are less mature at this juncture [36], and much work still remains in this area.

XIII. CONCLUSION

High-Q, third-order bandpass micromechanical filters have been designed and demonstrated in an IC-compatible polysilicon surface-micromachining technology. For design of these filters, electromechanical analogies proved very useful and facilitated the use of well-established LC ladder filter design principles and tables as starting points. Passband distortion due to the finite mass of coupling springs was shown to have significant impact on high-order filters, especially on the microscale, where resonators and couplers can have comparable

masses. Parasitic elements and process variations (mismatches) were also shown to more heavily influence the passband of high-order filters. Quarter-wavelength coupling beams, low velocity coupling, fully balanced operation, frequency-tunable resonators, and maximum electromechanical coupling can all greatly alleviate these nonideal effects and are key to successful microscale mechanical filter implementation. These design strategies will likely become increasingly important as the frequency and order of micromechanical filters rise to accommodate the needs of practical commercial transceivers.

APPENDIX A
RESONANCE FREQUENCY OF RATIOED FOLDED-BEAM MICROMECHANICAL RESONATORS

To aid in the derivation of the effective mass and stiffness of a ratioed folded-beam micromechanical resonator, Fig. 30 presents the shape of a ratioed folded-beam μresonator with shuttle displaced by a distance X_s under an applied force F_x in the x direction. Other relevant dimensions and variables are also included in the figure.

The frequency of a ratioed folded-beam μresonator can be approximated using Rayleigh's principle [20]

$$\text{KE}_{\text{max}} = \text{PE}_{\text{max}} \tag{A.1}$$

where KE_{max} and PE_{max} are the peak kinetic and potential energies achieved over a vibration cycle. Using Fig. 30

$$\text{KE}_{\text{max}} = \text{KE}_s + \text{KE}_{bi} + \text{KE}_{bo} + \text{KE}_t$$
$$= \frac{1}{2}\left[v_s^2 M_s + v_t^2 M_t + \int v_{bi}^2\, dM_{bi} + \int v_{bo}^2\, dM_{bo} \right] \tag{A.2}$$

where the M's represent previously defined *total* masses, and the v's represent peak velocities, with subscripts s, bi, bo, and t corresponding to the shuttle, the inner and outer folded-beams, and the folding trusses, respectively. With a peak velocity of $\omega_o X_s$, the peak kinetic energy for the shuttle can be written directly as

$$\text{KE}_s = \frac{1}{2}(\omega_o X_s)^2 M_s. \tag{A.3}$$

To determine the peak kinetic energies of the inner and outer folded-beams, the peak velocity as a function of location y must be determined for each. By considering stiffness relationships, these velocities can also be written in terms of the shuttle displacement X_s. Under fixed-fixed sliding boundary conditions, the stiffness of a flexural beam is given by [37]

$$k = \frac{12EI}{L^3} \tag{A.4}$$

where k is the stiffness of the beam, E is the Young's modulus of its material, $I = hW^3/12$ is the bending moment of inertia of the beam, and h, W, and L are its thickness, width, and length, respectively. Using (A.4), and with reference to Fig. 30, the stiffnesses of the inner and outer beams are related by

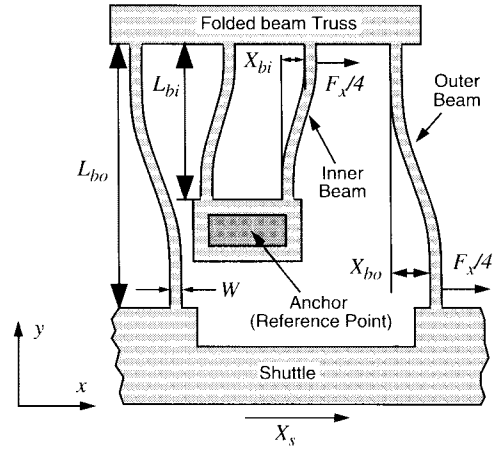$$\frac{k_{bo}}{k_{bi}} = \left(\frac{L_{bi}}{L_{bo}}\right)^3. \tag{A.5}$$

Fig. 30. Schematic presenting the shape of a ratioed folded-beam μresonator with shuttle displaced by a distance X_s under an applied force F_x in the x direction.

Given that the force in the spring system is divided evenly between each inner–outer beam pair, and the inner and outer beams of a given pair each see the same force equal to $F_x/4$, this stiffness ratio can also be written in terms of peak beam deflections

$$\frac{k_{bo}}{k_{bi}} = \frac{X_{bi}}{X_{bo}}. \tag{A.6}$$

Combining (A.5) and (A.6)

$$\frac{X_{bi}}{X_{bo}} = \left(\frac{L_{bi}}{L_{bo}}\right)^3 = \frac{1}{\beta^3} \tag{A.7}$$

where β is the ratio of the outer beam length L_{bo} to the inner beam length L_{bi}. With reference to Fig. 30

$$X_{bi} = \frac{X_s}{1 + \beta^3} \tag{A.8}$$

and the peak deflection profiles of the inner and outer beams as a function of y can now be expressed as [37]

$$x_{bi}(y) = \frac{X_s}{1 + \beta^3}\left[3\left(\frac{y}{L_{bi}}\right)^2 - 2\left(\frac{y}{L_{bi}}\right)^3 \right] \tag{A.9}$$

$$x_{bo}(y) = X_s\left\{ 1 - \frac{\beta^3}{1 + \beta^3}\left[3\left(\frac{y}{L_{bo}}\right)^2 - 2\left(\frac{y}{L_{bo}}\right)^3 \right] \right\} \tag{A.10}$$

from which the respective peak kinetic energies (for all the inner beams and all the outer beams, respectively) can be written

$$\text{KE}_{bi} = \frac{1}{2}\int_0^{L_{bi}} [\omega_o x_{bi}(y)]^2 \frac{M_{bi}}{L_{bi}}\, dy \tag{A.11}$$

$$\text{KE}_{bo} = \frac{1}{2}\int_0^{L_{bo}} [\omega_o x_{bo}(y)]^2 \frac{M_{bo}}{L_{bo}}\, dy. \tag{A.12}$$

Recognizing a truss velocity equal to $\omega_o X_{bi}$ and performing the needed integrations, the peak kinetic energy of the total

system is found to be

$$KE_{max} = \frac{1}{2}(\omega_o X_s)^2 \left(M_s + \frac{M_t}{(1+\beta^3)^2} + \frac{13}{35(1+\beta^3)^2}M_{bi} \right. $$
$$\left. + \left[\frac{1}{(1+\beta^3)} + \frac{13\beta^6}{35(1+\beta^3)^2} \right] M_{bo} \right\} \quad (A.13)$$

from which the effective mass at the shuttle can easily be identified as

$$m_{rs} = M_s + \frac{M_t}{(1+\beta^3)^2} + \frac{13}{35(1+\beta^3)^2}M_{bi}$$
$$+ \left[\frac{1}{(1+\beta^3)} + \frac{13\beta^6}{35(1+\beta^3)^2} \right] M_{bo}. \quad (A.14)$$

To find the peak potential energy of the system, an expression for the stiffness seen at the shuttle location is required. For this purpose, the deflection profile of the inner beam can be rewritten in terms of the applied force $F_x/4$ to yield [37]

$$x_{bi}(y) = \frac{F_x}{48EI}(3L_{bi}y^2 - 2y^3). \quad (A.15)$$

Evaluating (A.9) and (A.15) at $y = L_{bi}$, then equating them and solving, the stiffness at the shuttle location k_{rs} is found to be

$$k_{rs} = \frac{F_x}{X_s} = \frac{4Eh}{(1+\beta^3)}\left(\frac{W}{L_{bi}}\right)^3 \quad (A.16)$$

from which the peak potential energy in the system follows as

$$PE_{max} = \frac{1}{2}k_{rs}X_s^2 = \frac{2EhX_s^2}{(1+\beta^3)}\left(\frac{W}{L_{bi}}\right)^3. \quad (A.17)$$

Using (A.13) and (A.17) in (A.1), the resonance frequency of this ratioed folded-beam μresonator is finally found to be

$$\omega_o = \sqrt{\frac{k_{rs}}{m_{rs}}} = \left[\frac{4Eh(W/L_{bi})^3}{(1+\beta^3)m_{rs}} \right]^{1/2}. \quad (56)$$

ACKNOWLEDGMENT

REFERENCES

[1] H. Khorramabadi and P. R. Gray, "High-frequency CMOS continuous-time filters," *IEEE J. Solid-State Circuits*, vol. SC-19, pp. 939–948, Dec. 1984.

[2] K. B. Ashby, I. A. Koullias, W. C. Finley, J. J. Bastek, and S. Moinian, "High Q inductors for wireless applications in a complementary silicon bipolar process," *IEEE J. Solid-State Circuits*, vol. 31, pp. 4–9, Jan. 1996.

[3] N. M. Nguyen and R. G. Meyer, "Si IC-compatible inductors and LC passive filters," *IEEE J. Solid-State Circuits*, vol. 25, pp. 1028–1031, Aug. 1990.

[4] P. R. Gray and R. G. Meyer, "Future directions in silicon IC's for RF personal communications," in *Proc. IEEE Custom Integrated Circuits Conf.*, Santa Clara, CA, May 1–4, 1995, pp. 83–90.

[5] C. T.-C. Nguyen, L. P. B. Katehi, and G. M. Rebeiz, "Micromachined devices for wireless communications," *Proc. IEEE*, vol. 86, pp. 1756–1768, Aug. 1998.

[6] C. T.-C. Nguyen, "Frequency-selective MEMS for miniaturized low-power communication devices (invited)," *IEEE Trans. Microwave Theory Tech.*, vol. 47, pp. 1486–1503, Aug. 1999.

[7] W. C. Tang, T.-C. H. Nguyen, and R. T. Howe, "Laterally driven polysilicon resonant microstructures," *Sens. Actuators*, vol. 20, pp. 25–32, 1989.

[8] R. T. Howe and R. S. Muller, "Resonant microbridge vapor sensor," *IEEE Trans. Electron Devices*, vol. ED-33, pp. 499–506, 1986.

[9] C. T.-C. Nguyen and R. T. Howe, "Quality factor control for micromechanical resonators," in *Tech. Dig. IEEE Int. Electron Devices Conf.*, San Francisco, CA, Dec. 14–16, 1992, pp. 505–508.

[10] ———, "Microresonator frequency control and stabilization using an integrated micro oven," in *Dig. 7th Int. Conf. Solid-State Sensors and Actuators (Transducers'93)*, Yokohama, Japan, June 7–10, 1993, pp. 1040–1043.

[11] L. Lin, C. T.-C. Nguyen, R. T. Howe, and A. P. Pisano, "Micro electromechanical filters for signal processing," in *Tech. Dig. IEEE Microelectromechanical Systems Workshop*, Travemunde, Germany, Feb. 4–7, 1992, pp. 226–231.

[12] F. D. Bannon III, J. R. Clark, and C. T.-C. Nguyen, "High frequency microelectromechanical IF filters," in *Tech. Dig. IEEE Int. Electron Devices Conf.*, San Francisco, CA, Dec. 8–11, 1996, pp. 773–776.

[13] K. Wang and C. T.-C. Nguyen, "High-order micromechanical electronic filters," in *Proc. 1997 IEEE Int. Microelectromechanical Systems Workshop*, Nagoya, Japan, Jan. 26–30, 1997, pp. 25–30.

[14] K. Wang, F. D. Bannon III, J. R. Clark, and C. T.-C. Nguyen, "Q-enhancement of micromechanical filters via low-velocity spring coupling," in *Proc. 1997 IEEE Int. Ultrasonics Symp.*, Toronto, ON, Canada, Oct. 5–8, 1997, pp. 323–327.

[15] A. I. Zverev, *Handbook of Filter Synthesis*. New York: Wiley, 1967.

[16] A. S. Sedra and P. O. Brackett, *Filter Theory and Design: Active and Passive*. Beaverton, OR: Matrix, 1978.

[17] C. T.-C. Nguyen and R. T. Howe, "An integrated CMOS micromechanical resonator high-Q oscillator," *IEEE J. Solid-State Circuits*, vol. 34, pp. 440–445, Apr. 1999.

[18] Y.-H. Cho, A. P. Pisano, and R. T. Howe, "Viscous damping model for laterally oscillating microstructures," *IEEE J. Microelectromech. Syst.*, vol. 3, pp. 81–87, June 1994.

[19] R. A. Johnson, *Mechanical Filters in Electronics*. New York: Wiley, 1983.

[20] L. Meirovitch, *Analytical Methods in Vibrations*. New York: Macmillan, 1967.

[21] H. A. C. Tilmans, "Equivalent circuit representation of electromechanical transducers: I—Lumped-parameter systems," *J. Micromech. Microeng.*, vol. 6, pp. 157–176, 1996.

[22] T. B. Gabrielson, "Fundamental noise limits in miniature acoustic and vibration sensors," Phase Rep. NADC-91113-50, Dec. 31, 1991.

[23] ———, "Mechanical-thermal noise in micromachined acoustic and vibration sensors," *IEEE Trans. Electron Devices*, vol. 40, pp. 903–909, May 1993.

[24] H. Nathanson, W. E. Newell, R. A. Wickstrom, and J. R. Davis Jr., "The resonant gate transistor," *IEEE Trans. Electron Devices*, vol. ED-14, pp. 117–133, Mar. 1967.

[25] C. T.-C. Nguyen, "Micromechanical signal processors," Ph.D. dissertation, Dept. Elec. Eng. Comput. Sci., Univ. California-Berkeley, Dec. 1994.

[26] M. Konno and H. Nakamura, "Equivalent electrical network for the transversely vibrating uniform bar," *J. Acoust. Soc. Amer.*, vol. 38, pp. 614–622, Oct. 1965.

[27] H. Guckel, J. J. Sniegowski, R. T. Christenson, and F. Raissi, "The application of fine-grained, tensile, polysilicon to mechanically resonant transducers," *Sens. Actuators*, vol. A21, pp. 346–351, 1990.

[28] V. B. Braginskky, V. P. Mitrofanov, and V. I. Panov, *Systems with Small Dissipation*. Chicago, IL: Univ. of Chicago Press, 1985.

[29] C. T.-C. Nguyen, "Micromechanical resonators for oscillators and filters (invited)," in *Proc. IEEE Int. Ultrasonics Symp.*, Seattle, WA, Nov. 7–10, 1995, pp. 489–499.

[30] D. F. Sheahan and R. A. Johnson, *Modern Crystal & Mechanical Filters*. New York: IEEE Press, 1977.

[31] W. A. Johnson and L. K. Warne, "Electrophysics of micromechanical comb actuators," *IEEE J. Microelectromech. Syst.*, vol. 4, pp. 49–59, Mar. 1995.

[32] W. C. Tang, M. G. Lim, and R. T. Howe, "Electrostatic comb drive levitation and control method," *IEEE J. Microelectromech. Syst.*, vol. 1, pp. 170–178, Dec. 1992.

[33] J. W. Weigold, W. H. Juan, and S. W. Pang, "Dry etching of deep Si trenches for released resonators in a Cl$_2$ plasma," *J. Electrochem. Soc.*, vol. 145, pp. 1767–1771, 1998.

[34] K. S. Lebouitz, A. Mazaheri, R. T. Howe, and A. P. Pisano, "Vacuum encapsulation of resonant devices using permeable polysilicon," in *Tech. Dig. IEEE Int. Microelectromechanical Systems Workshop*, Orlando, FL, Jan. 17–21, 1999, pp. 470–475.

[35] M. M. Maharbiz, M. B. Cohn, R. T. Howe, R. Horowitz, and A. P. Pisano, "Batch micropackaging by compression-bonded wafer-wafer transfer," in *Tech. Dig. IEEE Int. Microelectromechanical Systems Workshop*, Orlando, FL, Jan. 17–21, 1999, pp. 482–489.

[36] K. Wang, A.-C. Wong, W.-T. Hsu, and C. T.-C. Nguyen, "Frequency-trimming and Q-factor enhancement of micromechanical resonators via localized filament annealing," in *Dig. Int. Conf. Solid-State Sensors and Actuators*, Chicago, IL, June 16–19, 1997, pp. 109–112.

[37] J. M. Gere and S. P. Timoshenko, *Mechanics of Materials*, 3rd ed. Boston, MA: PWS, 1990.

Kun Wang (S'95) received the B.S. degree in electrical engineering from the University of Electronic Science and Technology of China, Chengdu, China, in 1982, and the M.S. degree in electrical engineering from the University of Michigan, Ann Arbor, MI, in 1994, where he is currently working toward the Ph.D. degree.

From 1982 to 1991, he was a research engineer with Nanjing Electronic Devices Institute, Nanjing, China, involved in the development of highly sensitive night vision silicon imagers and thin film transistors for active matrix liquid crystal displays. Since 1992, he has been a Graduate Research Assistant with the Solid-State Electronics Laboratory at the University of Michigan, where he initially worked on the growth and characterization of wide bandgap semiconductors (GaN and AlN) and then on microelectromechanical signal processors for wireless communication applications. His current interests include sensors and systems, merged circuit/microelectromechanical technologies, and integrated circuit design and technology.
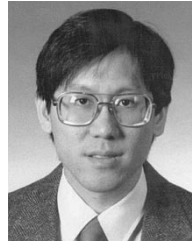
Clark T.-C. Nguyen (S'90–M'95) was born in Austin, TX, on March 29, 1967. He received the B.S., M.S., and Ph.D. degrees from the University of California at Berkeley in 1989, 1991, and 1994, respectively, all in electrical engineering and computer sciences.

In 1995, he joined the faculty of the University of Michigan, Ann Arbor, MI, where he is currently an Assistant Professor in the Department of Electrical Engineering and Computer Science. From 1995 to 1997, he was a member of the National Aeronautics and Space Administration's (NASA) New Millennium Integrated Product Development Team on Communications, which roadmaps future communications technologies for NASA use into the turn of the century. His research interests focus upon microelectromechanical systems and include integrated micromechanical signal processors and sensors, merged circuit/micromechanical technologies, RF communication architectures, and integrated circuit design and technology.

Prof. Nguyen received the 1938E Research and Teaching Excellence Award from the University of Michigan in 1998, an EECS Departmental Achievement Award in 1999, and was a Finalist for the 1998 Discover Magazine Technological Innovation Awards. Together with his students, he received the Roger A. Haken Best Student Paper Award at the 1998 IEEE International Electron Devices Meeting, and the Judges' Award for Best Paper at the 1998 IEEE MTT-S International Microwave Symposium. He recently co-chaired the Workshop on Microelectromechanical Devices for RF Systems at the 1999 IEEE MTT-S Symposium.